Title: Quantitative modelling of biological response dynamics reveals novel patterns in plant volatile signalling

Authors: Jamie M. Waterman*†[1,2], Gareth J. Moore†[3], Loren K. Amdahl-Culleton[3], Sara Hoefer[2], Matthias Erb[2]

Affiliations: [1]Discipline of Botany, School of Natural Sciences, Trinity College Dublin, Dublin, Ireland

[2]Institute of Plant Sciences, University of Bern, Bern, Switzerland

[3]Independent

*Corresponding author. Email: watermaj@tcd.ie

†Authors contributed equally to this work

Abstract:

Biological responses to environmental stimuli are inherently dynamic. Recent technological advances enable detailed time-resolved measurements of such responses. However, a unifying model for the quantitative characterisation of dynamic response curves is lacking, thus limiting biological insights and comparisons. We developed an unbiased mathematical modelling approach that allows for the quantitative characterisation of biological response curves without *a priori* knowledge of underlying biochemical mechanisms. Using stress-induced plant volatile emissions, we show that the model performs well across a wide range of datasets, including incomplete induction curves, curves with low sampling resolution and complex multi-modal responses that result from overlapping stimuli. Using the model, we uncover a range of previously unrecognised patterns in volatile induction curves, including i) a strong light-independent impact of the time of day of wounding on the onset, duration and shape of the volatile induction responses, ii) an accentuation of volatile-specific induction curve shapes by herbivory-associated molecular patterns (HAMPs) and iii) independent regulation of the strength and duration of volatile induction across genotypes. We conclude that our model allows for the quantitative analysis of dynamic response curves and can identify new biological response patterns. The presented approach will pave the way to characterising dynamic organismal responses across the tree of life.

Introduction

Inducible biological responses are transient in nature and change substantially over relatively short periods of time (*1–5*). By consequence, real-time measurements are crucial to understand physiological processes, precisely diagnose chronic and acute stress patterns and resolve ecological phenomena (*6–11*). Although biological processes are inherently dynamic, quantitatively describing and comparing temporal features of biological responses remains a challenge. It is well established that static features such as mean concentration at a given instance are useful for general interpretations of stimulus-response relationships, such as the inverse relationship between viral load and effective immune response in humans and the positive relationship between herbivore damage and volatile emissions in plants (*12*, *13*). However, static, nominal values, even if measured at different time points, ignore meaningful, quantifiable features of the dynamics themselves.

Recent examples illustrate the potential of moving beyond measures such as concentration or abundance to generate new biological insights. In plants, variation in the spatial distribution of a toxic metabolite, either within a plant or between plants, can affect herbivore feeding behaviour and thus fitness parameters such as growth, independently from the total concentration of said toxin (*14–16*). In animals, dendritic signals are sensitive to temporal patterns of synaptic activation; irrespective of the amount of signal, the temporal patterns of signal perception shape spike outputs, which drive crucial functions such as sound localisation (*17*, *18*). Additionally, the interaction between vaccination status, viral exposure and immune responses are all temporally linked, and the effects/response of each will be dependent on how the others change over time (*19*).

From a mechanistic perspective, the dynamics of biological responses are determined by the interplay of highly regulated signalling events (*20–25*) and modifications to one or more events

can have far-reaching consequences on response dynamics and metabolic outcomes (*1*, *17*, *26–28*). For diffusion-based processes such as generation of reactive oxygen species (ROS) or single-cell signalling events like MAPK cascades, the underlying steps are few and well-characterised, and relatively simple, real-time mechanistic models have been developed (*6*, *29–32*). Some models of temporal dynamics of metabolism with more complex biosynthetic pathways have also been developed (*33*, *34*). These models are valuable for elucidating biochemical mechanisms and understanding the complexity of metabolic regulation. However, they require substantial *a priori* biochemical knowledge and the ability to measure numerous kinetic and regulatory parameters (steps), making their construction challenging even for well-characterised metabolic processes (*35–37*). For more complex and less-well characterised pathways, such as the *de novo* production of specialised metabolites, complete time-resolved mechanistic models are not currently feasible. Many underlying processes, including enzyme kinetics, precursor and product concentrations, transport delays, degradation pathways and other regulatory processes remain unknown (*38–40*). Because the biochemistry is not fully defined, the number and nature of parameters required to describe such processes are effectively arbitrary, leading to under-constrained models in which multiple parameter combinations can reproduce the same behaviour and limit reliable fitting and meaningful interpretation (*37*). Moreover, existing models are often system-specific and must be adapted depending on the metabolites or pathways studied. Consequently, there is no universally standardised framework or parameterisation that can be easily implemented across systems, which limits comparability, broader applicability and ultimately accessibility of dynamic metabolite analyses.

Mechanistically informed models may not always be necessary to study biological responses. Volatile chemical signals emitted by organisms shape important interactions such as those between insects and their hosts (*41*, *42*). In this case, the mechanism of volatile formation

matters less than when this chemical information is released, how long it persists and whether amounts produced cross perceptual thresholds (*10*, *43–45*). These characteristics are also important for within-organism biochemical processes. Consider protein structural dynamics (i.e., moving between different conformational states in time), for which similar dynamic features would determine interactions with other proteins and metabolites, and thus shape the fate of biochemical processes (*46*, *47*). Thus, extracting time-resolved features of response dynamics that are intuitive, broadly comparable and important for driving biological functions becomes important. Both statistical and theoretical methods for modelling dynamic biological responses have been proposed (*8*, *13*, *19*). However, a universal model that enables quantitatively rigorous and biologically informative comparison of dynamic response features, either across stimuli or across systems, has yet to be developed.

Motivated by the lack of such a framework to quantitatively compare dynamic biological responses, we set out to develop a method that allows for meaningful, robust and consistent comparisons of dynamic responses without explicit knowledge of the underlying physiochemical and biochemical processes. We then generated a series of plant stress response datasets to test our method and evaluate whether it can generate new insights into biological responses. We considered plant stress responses, including induced volatiles, to be an optimal test case, as plants have evolved a highly complex array of responses to environmental stimuli, that cover a broad range of physiological and ecological functions (*48*), and show starkly distinct kinetics (*42*). Induced volatiles in particular can be measured non-destructively, enabling diverse processes to be observed in real time (*7*). Finally, plant metabolites serve as important chemical information for the wider environment, and we thus assumed that the generated insights would be informative on a biological and ecological level (*10*, *45*). The results demonstrate that our method is useful to compare biological responses.

Most importantly, it allowed us to uncover differences in plant stress response dynamics that would not be captured with traditional approaches, thus resulting in novel insights into the specificity and variation of biological responses. As the method is not specific to either response type or timeframe, it will be applicable over a broad range of dynamic processes across biological systems, thus unlocking novel comparative and integrative approaches across the tree of life.

Results

Model development

To build a phenomenological model that captures dynamic responses in an unbiased manner, we modelled responses as a distribution of waiting times. We asked the question: *How long does it take for a response unit (e.g. a volatile molecule) to appear following a stress event?* In doing so, we interpret each measured unit as a probabilistic occurrence with a certain delay, and thus model the response curve as a probability density function.

This framing is advantageous for three reasons: first, the model yields a relatively small number of parameters that are both identifiable (i.e. are intuitive by eye) and interpretable (i.e. have biological meaning). This minimises overfitting and, as a result, makes the model robust to sample-to-sample variation. Secondly, it enables comparability across responses which involve very different mechanisms and timeframes. Thirdly, the same framework can be applied to any induced phenotype that can be measured quantitatively over time, such as gene expression, hormone accumulation, enzymatic conversions, volatile emissions and resistance induction, even if they show starkly different dynamics and biosynthetic processes, as they all typically exhibit the same behaviour: induction delay following stimulation and a rapid increase in response, which, after reaching a peak, gradually declines (*1*, *2*, *28*, *49–57*). This is

mathematically intuitive as these responses are built from a sequential chain (or combinatory network) of activation, synthesis, transport and eventually measurement/detection. Each step adds stochastic waiting time with their sum naturally producing a skewed, unimodal distribution (*58*). Modelling this kind of process usually involves treating each biochemical step as a stochastic waiting time drawn from a defined probability distribution and then combining these into a final waiting-time distribution which captures the total observed response dynamics. As such, we used a reparametrised gamma distribution, which retains its form when steps are combined and can thus describe both early and later phases of the response in a consistent way (see materials and methods for full model details):

$$R(t) = R_{\text{peak}} \cdot \left(\frac{t - t_{\text{onset}}}{t_{\text{peak}} - t_{\text{onset}}}\right)^{\left(\frac{t_{\text{mean}} - t_{\text{onset}}}{t_{\text{mean}} - t_{\text{peak}}} - 1\right)} \cdot \exp\left(\frac{-\left(t - t_{\text{peak}}\right)}{t_{\text{mean}} - t_{\text{peak}}}\right)$$

where:

- R_{peak} is the maximum measured response,
- t_{onset} is the onset delay,
- t_{peak} is the time of peak response,
- t_{mean} is the mean response time.

The fitting parameters can then be used to calculate additional characteristic parameters (Fig 1A).

Total response ($Integral$) – The integral is often difficult to measure experimentally; due to time limitations in the measurement processes, entire curves are not resolved and thus incomplete integrations are used (*59*). When fit onto the experimental data, our model can be used to calculate the theoretical integral of the response curve even if it is incomplete:

$$\text{Integral} = R_{peak}\left(t_{mean} - t_{peak}\right)^{1+\frac{t_{peak}-t_{onset}}{t_{mean}-t_{peak}}} e^{\frac{t_{peak}-t_{onset}}{t_{mean}-t_{peak}}} \left(t_{peak} - t_{onset}\right)^{-\frac{t_{peak}-t_{onset}}{t_{mean}-t_{peak}}} \Gamma\left(1 + \frac{t_{peak} - t_{onset}}{t_{mean} - t_{peak}}\right)$$

where Γ() is the Gamma function, a continuous generalisation of the factorial (*46*, *47*).

$Duration$ – For response dynamics, response length is typically defined as 'broadness', for example as full width at half max (FWHM) (*6*). The FWHM of the Gamma function has no analytical solution and must be determined numerically (*62*). Additionally, FWHM, does not explicitly capture the start of the response. For these reasons $Duration$ is used as a simple alternative, achieving a similar descriptive value and used as a normalisation value in the 'shape' feature below.

$$Duration = t_{mean} - t_{onset}$$

$Shape$ – The 'shape' of a response curve is an abstract feature. Since our model is intended to be used over variable time scales, we developed a time-normalised (by $Duration$) metric that allows for comparison of curve shapes independently from response length. Further, we aimed to understand the symmetry of the curve in response to different stimuli or across plant genotypes/species to broadly assess temporal nuances. $Shape$ presents a new phenotypic axis which may link to important biochemical or physiochemical properties that regulate induced responses. $Shape$ is a normalised value, and when responses follow gamma distributions it falls between zero and one; a $Shape$ of zero indicates a perfectly symmetrical curve ($t_{mean} = t_{peak}$) and a shape of one represents a completely right-skewed curve ($t_{peak} = t_{onset}$):

$$Shape = \frac{t_{mean} - t_{peak}}{t_{mean} - t_{onset}}$$

188 Taken together, the fit and derived parameters give a framework for comparing curves,
189 particularly those that appear distinct by eye but are difficult to distinguish quantitatively (Fig
190 1B).

191

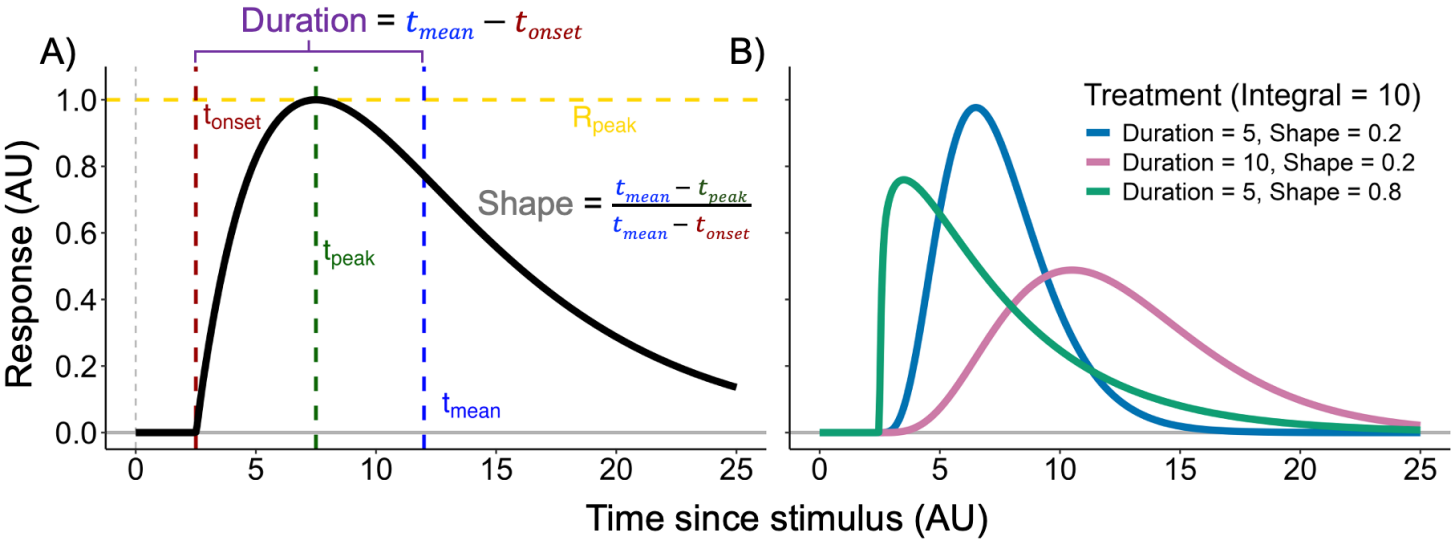

Figure 1. Theoretical examination of important features of biological response curves. A) Parameters of the model include t_{onset}: onset delay, t_{peak}: time of peak response, t_{mean}: mean response time, R_{peak}: the maximum measured response. These parameters are further reparametrised into $Duration$: metric of the length of response and $Shape$: our symmetry feature, which for gamma-like distributions falls between zero and one. B) *In silico* data highlighting the utility of model parameters, namely that discrete temporal response patterns can emerge, despite identical integrals.

192

193 <u>Uncovering novel patterns in plant volatile responses</u>

194 To explore the usefulness of the model, we measured inducible volatile emissions in maize
195 (*Zea mays*) in real-time by PTR-ToF-MS following different stress treatments. We focused
196 principally on the homoterpene 4,8-dimethylnona-1,3,7-triene (DMNT) as a highly inducible,
197 ecologically relevant plant volatile (*63–65*).

198 First, we tested whether the amount of mechanical leaf damage influences DMNT induction.
199 Earlier work showed that damage intensity strongly correlates with terpene emissions (*12*).
200 Indeed, higher damage increased total DMNT emissions DMNT (Fig. 2A), and our model

201 faithfully captured this pattern through $Integral$ (Fig 2B). No clear patterns were detected for
202 the other parameters, apart from differences in $Duration$, which was marginally longer for
203 intermediate amounts of wounding (Fig. 2D).

204 Next, we tested the influence of the circadian clock on wound-induced DMNT by wounding
205 plants at different times of day under continuous light. The circadian clock is known to play a
206 role in regulating how plants respond to stress, including transcriptional regulation of defence
207 genes (*66*, *67*). Time of day had no impact on the overall amount of DMNT emission (Fig 2G).
208 However, t_{onset}, $Duration$ and $Shape$ all varied significantly; wounding in the evening
209 resulted in a significantly more rapid, shorter DMNT burst – a novel pattern that has not been
210 reported before (Fig. 2F-J).

211 We also tested the influence of insect oral secretions (OS), which contain both elicitors and
212 effectors which can increase and decrease responses compared to wounding alone, respectively
213 (*68*). We confirmed that OS enhance the total emission of DMNT (Fig 2K-L). Interestingly,
214 OS treatment also led to a more rapid and prolonged response, resulting in a significantly
215 different curve shape (Fig 2M-O).

216 Leaf size and developmental stage can influence total volatile emissions (*49*), but whether these
217 parameters also influence response curves in other ways is unknown. We thus reanalysed the
218 dataset from our earlier work with our model. We found that leaf 3 (largest size and
219 intermediate age) emits volatiles for the longest period (Fig 2S). Interestingly, leaf 2 (older
220 leaf), despite producing more volatiles than leaf 4 (youngest leaf), did not produce them for a
221 longer period (Fig 2R). $Shape$ followed a clear developmental gradient, whereby older leaves
222 had more asymmetrical DMNT emission dynamics compared to younger leaves (Fig 2T).

223 Different genotypes vary strongly in the amount and type of volatiles they emit (*69*), but
224 whether response curves are also different is unknown. We determined response curves in three

225 maize inbred lines that differ in their capacity to produce DMNT (Fig 2U). As expected,
226 $Integral$ varied for all genotypes (Fig 2V). Interestingly, we found that higher emitting
227 genotypes also had substantially earlier t_{onset} (Fig 2W), however higher emissions do not
228 necessarily equate to earlier onsets (Fig 2A-C). Additionally, the two highest emitting
229 genotypes, CML287 and NC300, had similar $Duration$ (Fig 2X) and CML287 had the most
230 symmetrical dynamics. Thus, different genotypes show starkly different response patterns,
231 some of which are independent of total volatile quantity. Taken together, these experiments
232 illustrate the power of our approach to uncover novel, genetically determined response patterns
233 to environmental stimuli.

234

235 Unravelling differences between biochemically distinct compound classes

236 To explore the usefulness of our model to compare different types of response curves, we
237 characterised volatiles from different biosynthetic pathways, including terpenes, indole and
238 green leaf volatiles (*1*). In response to wounding, the different volatiles exhibited significantly
239 different response curves, as described before, which was visible in differences in t_{onset},
240 $Duration$ and $Shape$ (Fig. 3A-E; Fig S1). Interestingly, the differences became more
241 pronounced with the application of OS (Fig. 3F-J). This pattern was most clearly visible in the
242 $Shape$ parameter: while in the absence of OS, all compounds except monoterpenes had a
243 similar $shape$, all but DMNT and TMTT developed their own unique $shape$ when induced by
244 OS (Fig 3E and J), illustrating that OS components act differently on different volatile
245 pathways.

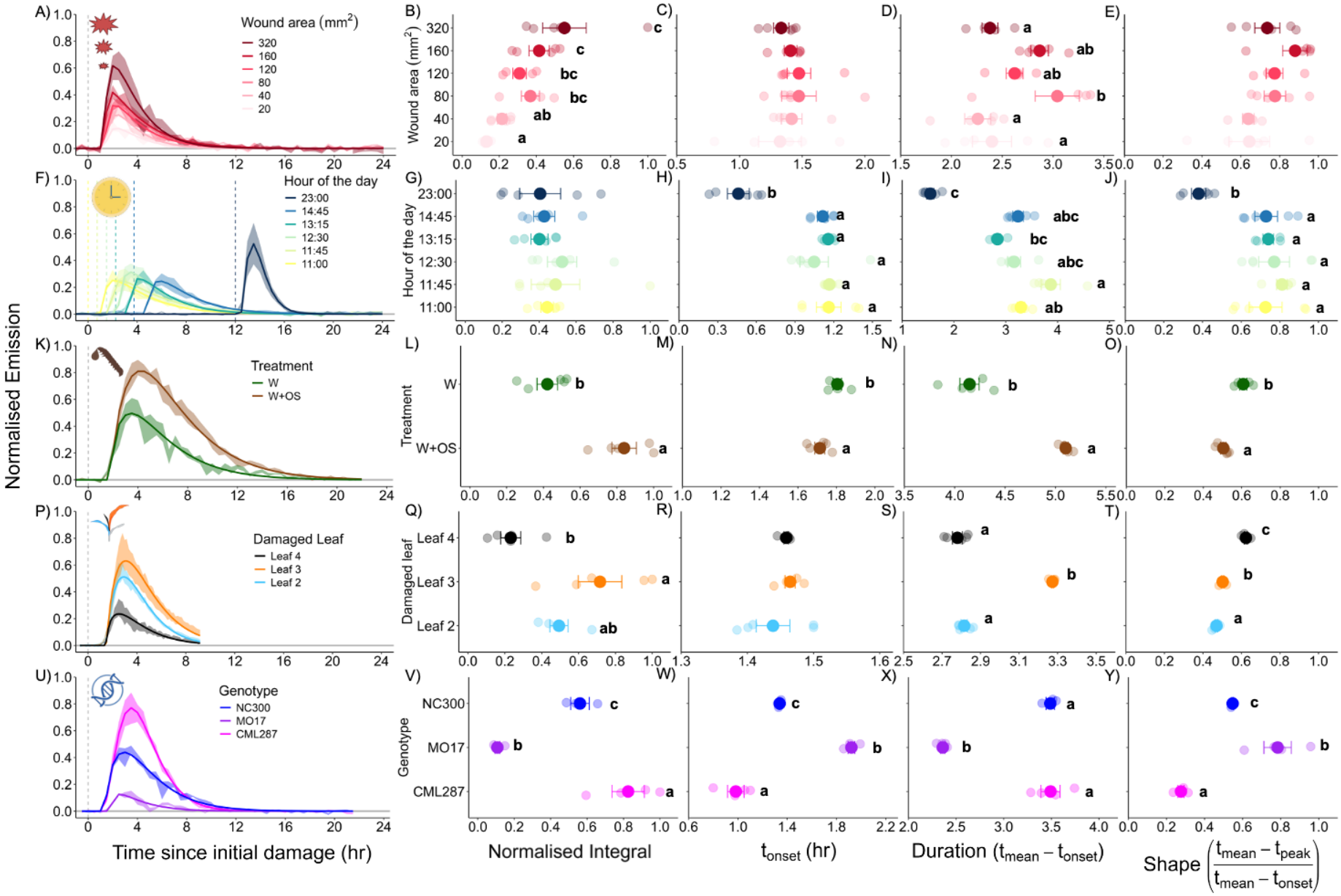

Figure 2. Application of the model to compare volatile emission dynamics in response to a range of stimuli. Each horizontal row of panels represents a unique experiment. A-E) responses to variable wounding intensities, F-J) responses to the same intensity of damage at different times of day (Note: t_{onset} is standardised based on time of damage), K-O) responses compared between wounded plants and plants treated with wounding and *Spodoptera exigua* oral secretions (OS), P-T) responses to damage in leaves of different developmental stages (Data from Waterman et al., 2025), U-Y) wounding responses compared between genotypes with highly variable volatile emission capacity. For the first column of panels, curves depict emission data, where the solid line represents mean of fitted emission across biological replicates and the translucent ribbon represents the baseline-subtracted raw emission data ± SE. For the remaining columns, solid points represent mean values across biological replicates (translucent points). Error bars represent SE. Within each panel, different letters indicate significant differences between groups as determined by multiple comparisons tests following significant ($p < 0.05$) one-way ANOVA or Kruskal-Wallis tests. n = 4-6.

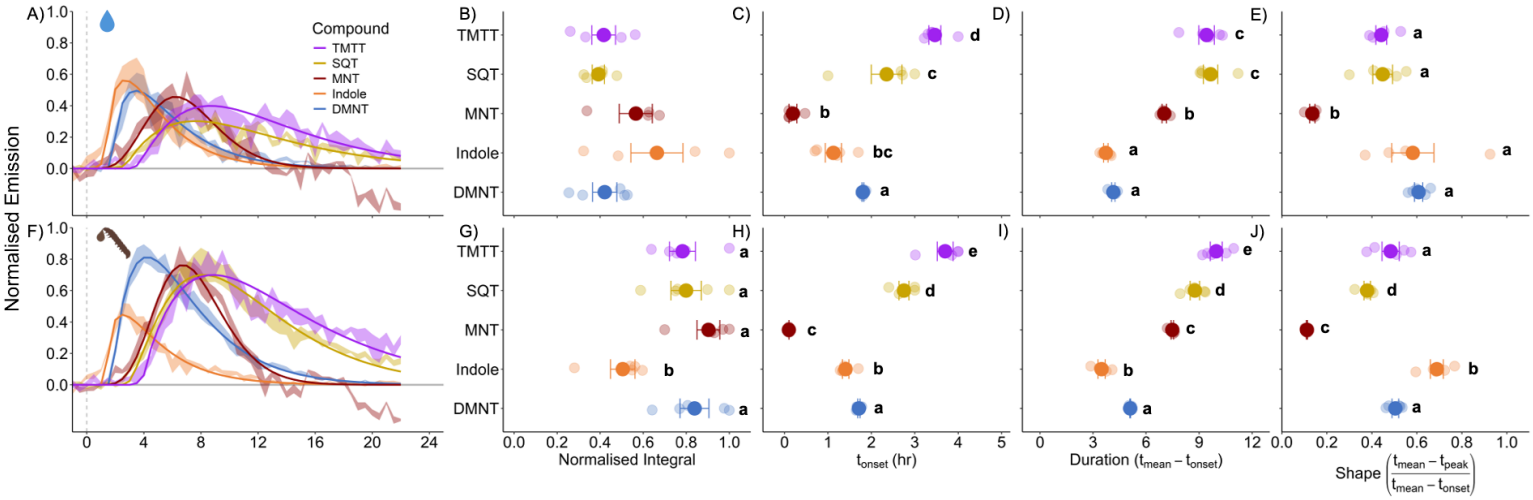

Figure 3. Impacts of herbivore-specific stimuli on volatile emission dynamics. Emission and model parameters for wounded plants (A-E) and wounded plants treated with oral secretions (OS; F-J). For the first column of panels (A and F), curves depict emission data, where the solid line represents mean of fitted emission across biological replicates and the translucent ribbon represents the baseline-subtracted raw emission data ± SE. For the remaining columns, solid points represent mean across biological replicates (translucent points). Error bars represent SE. Within each panel, different letters indicate significant differences between groups as determined by multiple comparisons tests following significant ($p < 0.05$) one-way ANOVA. $n = 4$-5. Abbreviations: DMNT= 4,8-dimethylnona-1,3,7-triene, MNT = monoterpenes, SQT = sesquiterpenes, TMTT = 4,8,12-trimethyltrideca-1,3,7,11-tetraene.

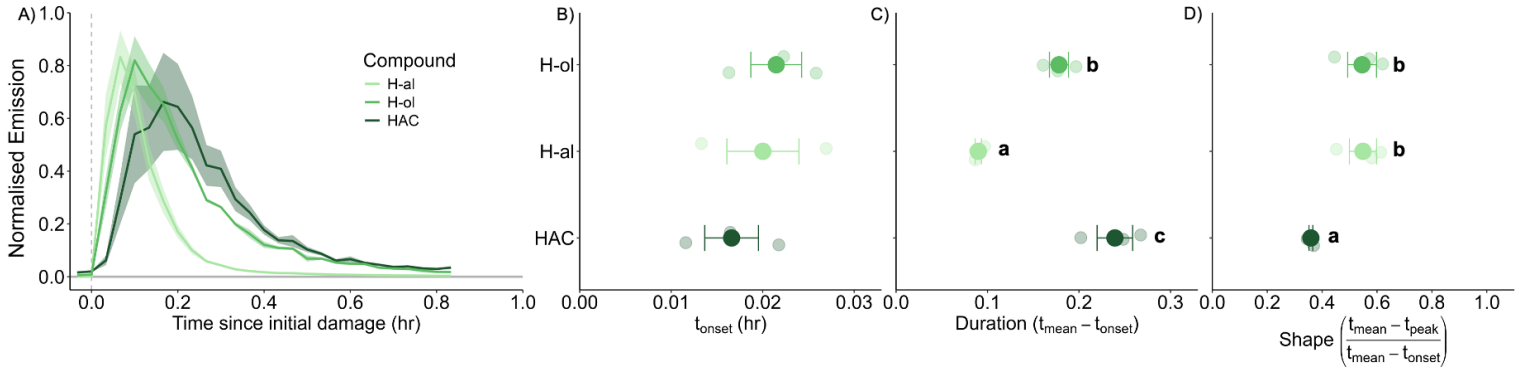

Supplemental Figure 1. Dynamics of green leaf volatile (GLV) emissions. For A) curves depict emission data, where the solid line represents mean of fitted emission across biological replicates and the translucent ribbon represents the baseline-subtracted raw emission data ± SE. For the remaining columns, solid points represent mean across biological replicates (translucent points). Error bars represent SE. Within each panel, different letters indicate significant differences between groups as determined by multiple comparisons tests following significant ($p < 0.05$) one-way ANOVA. $n = 3$. Abbreviations: H-al = hexenal, H-ol = hexenol, HAC = hexenyl acetate.

252 To explore this phenomenon more deeply and test our model on a less temporally resolved
253 dataset, we modelled the gene expression dynamics of *ZmCYP92C5*, *ZmIGL, ZmTPS2* and
254 *ZmTPS10* (Fig S2), which are coding for the rate limiting enzymes of the biosynthesis pathways
255 of DMNT/TMTT, indole, monoterpenes and sesquiterpenes (*49*). Trends in $Duration$ of these
256 genes matched emission of corresponding volatiles (Fig S2C), confirming that volatile
257 emission is regulated by biosynthetic limitations (Fig S2; *12*, *56*). No differences in gene
258 expression were found for t_{onset} and $shape$ (Fig S2B and D), possibly due to a lack of
259 resolution of expression dynamics (Figs S3 and S4).

260

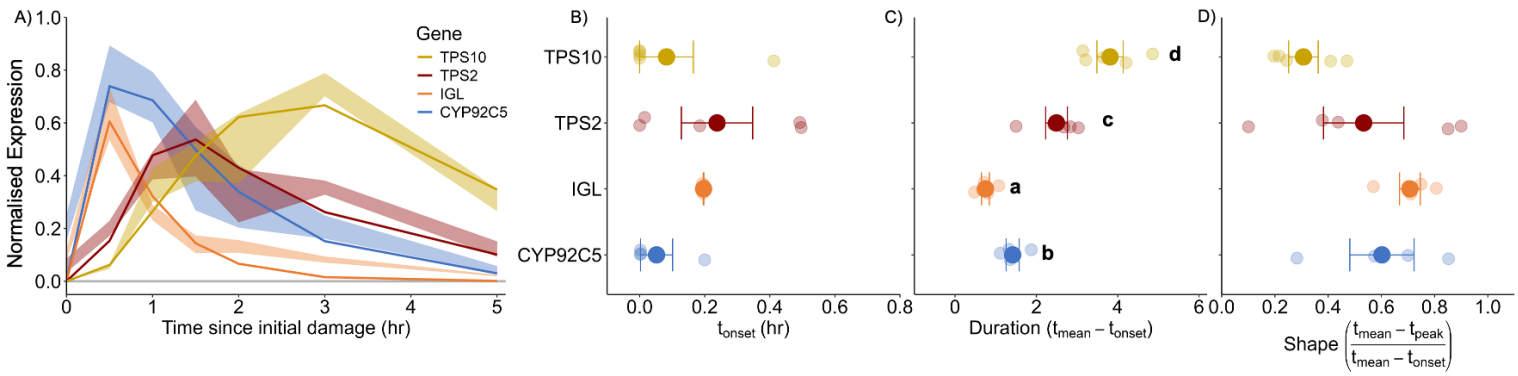

Supplemental Figure 2. Volatile biosynthesis gene expression dynamics. For A), curves depict baseline-subtracted raw expression data, where the solid line represents mean of fitted expression across biological replicates and the translucent ribbon represents the baseline-subtracted raw expression data ± SE. For the remaining columns, solid points represent mean across biological replicates (translucent points). Error bars represent SE. Within each panel, different letters indicate significant differences between groups as determined by multiple comparisons tests following significant ($p < 0.05$) one-way ANOVA. n = 4-5. Abbreviations: CYP92C5 = dimethylnonatriene/trimethyltetradecatetraene synthase, IGL = indole-3-glycerol phosphate lyase, TPS2 = terpene synthase 2, TPS10 = terpene synthase 10 .

261

262

263 <u>Exploring complex damage and response patterns</u>

264 To test the ability of our model to characterize more complex induction patterns, we measured
265 volatile emissions following multiple wounding events (Fig 4A). The current assumption from
266 the literature is that subsequent wounding should lead to stronger defence responses beyond

cumulative effects, as the earlier wounding will prime plants for subsequent responses. However, such effects have been hard to isolate for wounding events that follow each other closely in time due to overlapping response curves. Thus, we modelled the responses to three wounding events as the sum of three separate curves, all of which being effectively incomplete or not fully resolved in some way. By decomposing the overall emission into separate fitted curves, we were able to quantify the dynamic contribution of each individual wounding event, even when the peaks overlapped. This revealed a clear priming effect where the $integral$ of the second and third responses were larger than that of the initial peak, demonstrating that prior damage enhanced subsequent emissions beyond additive effects (Fig 4B). At this particular time interval, multiple damage events did not significantly modify other fit parameters (Fig 4C-E). The functionality of this model on more complex damage patterns highlights its utility to explore response dynamics under complex stress regimes.

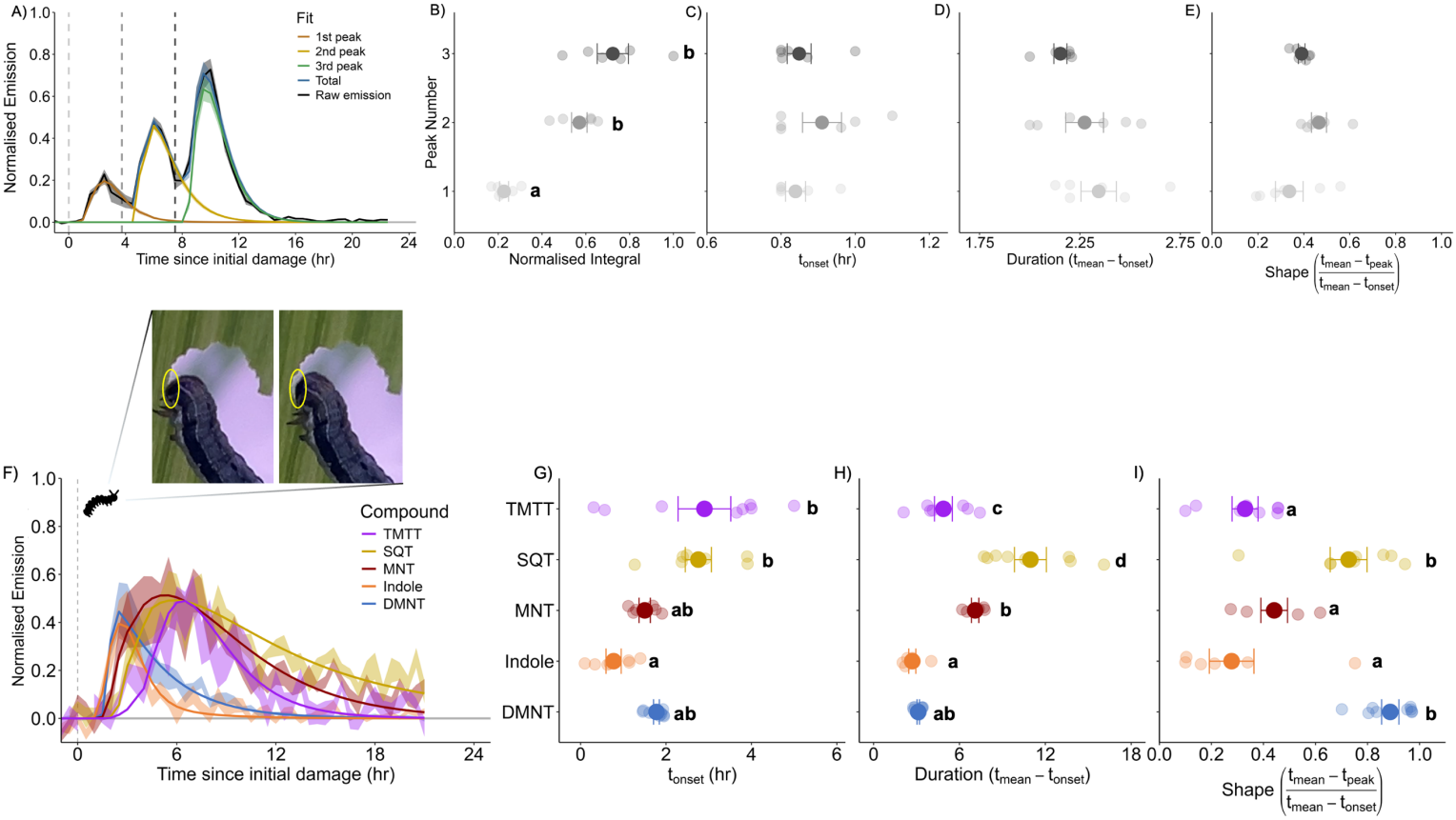

Figure 4. Fitting responses to complex stimuli patterns. A) Fitted emission for each curve plotted over total fitted emission and baseline-subtracted raw emission B-E) Model parameters for each peak. F) Curves depict emission data and G-I depict model parameters from *Spodoptera exigua*-infested plants. For A and F, the translucent ribbons represent the baseline-subtracted raw emission data ± SE from the respective, colour-coded curve. For B-E and G-I, solid points represent mean across biological replicates (translucent points). Error bars represent SE. Within each panel, different letters indicate significant differences between groups as determined by multiple comparisons tests following significant one-way ANOVA. For A-E, n = 6 and for F-I, n = 6-8. Abbreviations: DMNT= 4,8-dimethylnona-1,3,7-triene, MNT = monoterpenes, SQT = sesquiterpenes, TMTT = 4,8,12-trimethyltrideca-1,3,7,11-tetraene.

Herbivores do not make single wounds when they feed, but rather take many bites over time. To test the application of the model under realistic conditions, we fit it to response curves to feeding by a single *Spodoptera exigua* larva for 30 min. Natural herbivory patterns generated responses that could easily be fitted for all groups of volatiles (Fig 4F). t_{onset} showed some similarities to wounding response patterns, namely that sesquiterpenes and TMTT take longer to begin emitting than other compounds (Fig 4G). Interestingly, $Duration$ values more closely matched those from simple wounding than wounding + OS (Fig 4H). $Shape$ values showed

288 stark differences compared to wounding treatments, suggesting that damage patterns may play
289 an important role in determining response curves (Fig 4I). The ability to effectively fit
290 parameters to responses induced by real herbivore feeding indicates that our model is functional
291 even when exact damage patterns and timing are not known, and thus it can be used widely.

292

293 Modelling incomplete curves

294 Understanding the dynamics of defence responses requires some level of continuous
295 monitoring. However, how the temporal resolution of measurements impacts the capacity to
296 understand dynamic patterns is not well known. We tested the sensitivity of our model to
297 measurement duration and sampling resolution. Firstly, in order to simulate a shorter
298 measurement window, we removed datapoints from the end of the curve (in time) and
299 compared fit parameters to those from the complete dataset. For $integral$ and $duration$,
300 there was a consistent point around t_{mean} where removal of data dramatically reduce the
301 accuracy of model parameters (Fig S3B, G and L). t_{onset} was more sensitive to data removal
302 for indole and TMTT than it was for DMNT (Fig S3C, H and M). Similarly for $shape$, which
303 is t_{onset}-dependent), indole and TMTT fits broke down relative to the complete dataset with
304 less data removal than DMNT (Fig S3E, J and O). Interestingly, for DMNT and indole, even
305 with removal of *ca.* 10-15 hr of curve the fitted parameters remained almost entirely stable, if
306 not identical, suggesting a substantial degree of flexibility and potential to understand the
307 dynamics of only partially resolved peaks.

308 Second, we tested the resolution tolerance of the model by periodically removing datapoints,
309 simulating a lower resolution measurement (Fig S4A, F and K). With periodic removal of up
310 to 85% of data points, the emission $integral$ was able to be recovered with nearly the same
311 accuracy and precision for all compounds, suggesting that a coarse 'outline' of temporal

response patterns can be sufficient to accurately estimate total emissions over time (Fig S4B, G and L). For indole, removal of 70% data in periodic intervals resulted in breakdown of $integral$ as the overall curve structure was nearly entirely lost (Fig S4B). Indole has the fastest emission dynamics, and as such, indole has the lowest effective resolution in comparison to DMNT and TMTT, which both have slower kinetics and thus more data points between t_{onset} and t_{mean}. Interestingly, for other fit parameters (t_{onset}, $duration$ and $shape$), accuracy and precision began to consistently breakdown at 70% removal, suggesting there is a limit to measurement frequency for certain dynamic features (Fig S4). Overall, indole appeared to be the most susceptible to reduced resolution, again, likely due to indole's faster dynamics and lower effective resolution. Importantly, these results highlight that response kinetics are a necessary consideration to determine the use of truly 'continuous' measurements; they may not always be required or even provide additional dynamic information.

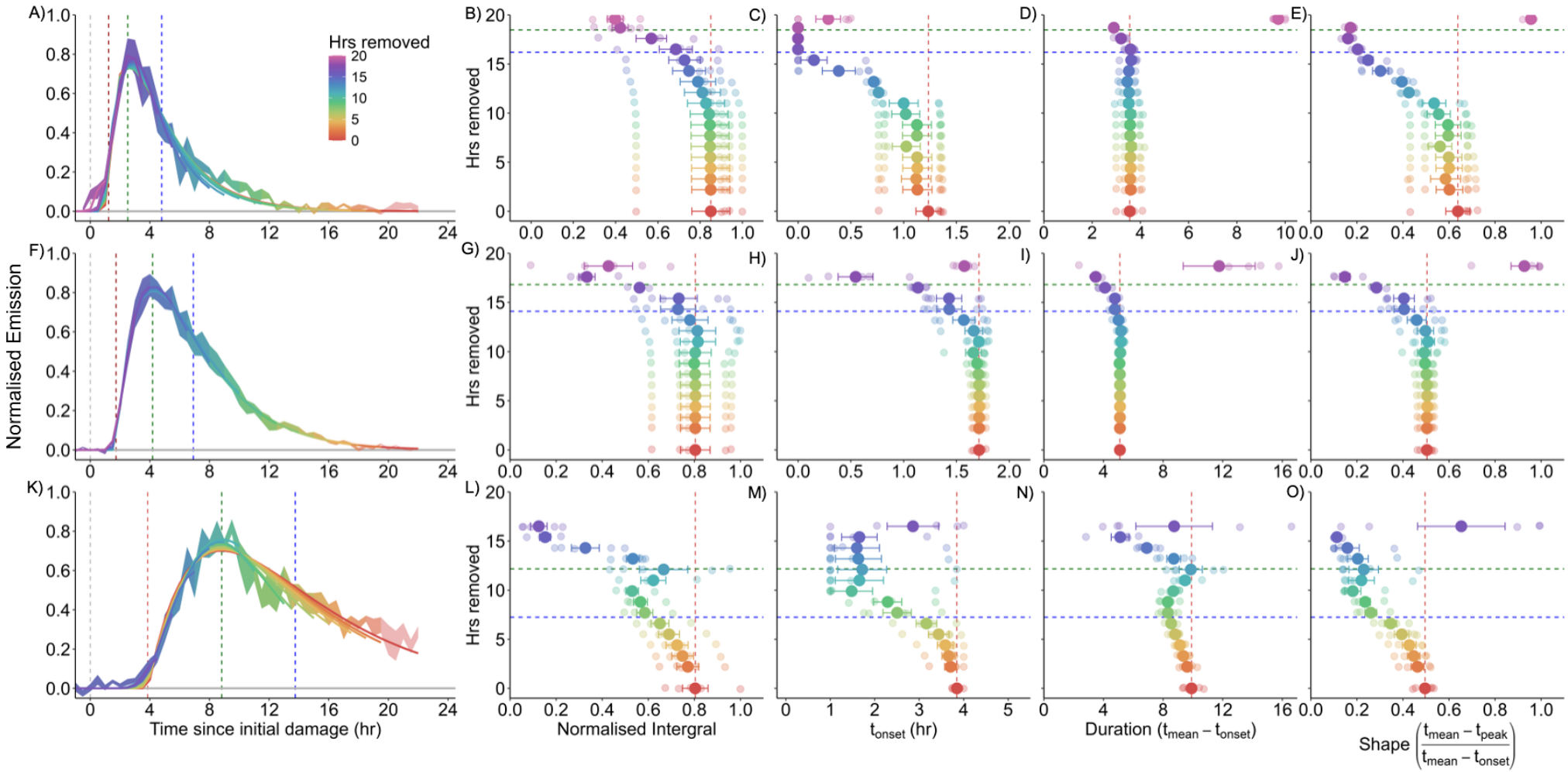

Supplemental Figure 3. Fitting incomplete response curves. Emission and fit parameters for A-E) indole, F-J) DMNT and K-O) TMTT. For the first column of figures, curves depict emission data, where the each solid line represents mean of fitted emission across biological replicates and the translucent ribbon represents the raw baseline-subtracted emission data ± SE. For the remaining columns, solid points represent mean across biological replicates (translucent points). Error bars represent SE. Colour gradient indicates the number of hours removed from the back end of the curve. *n* = 5-6. Abbreviations: DMNT= 4,8-dimethylnona-1,3,7-triene, TMTT = 4,8,12-trimethyltrideca-1,3,7,11-tetraene.

331

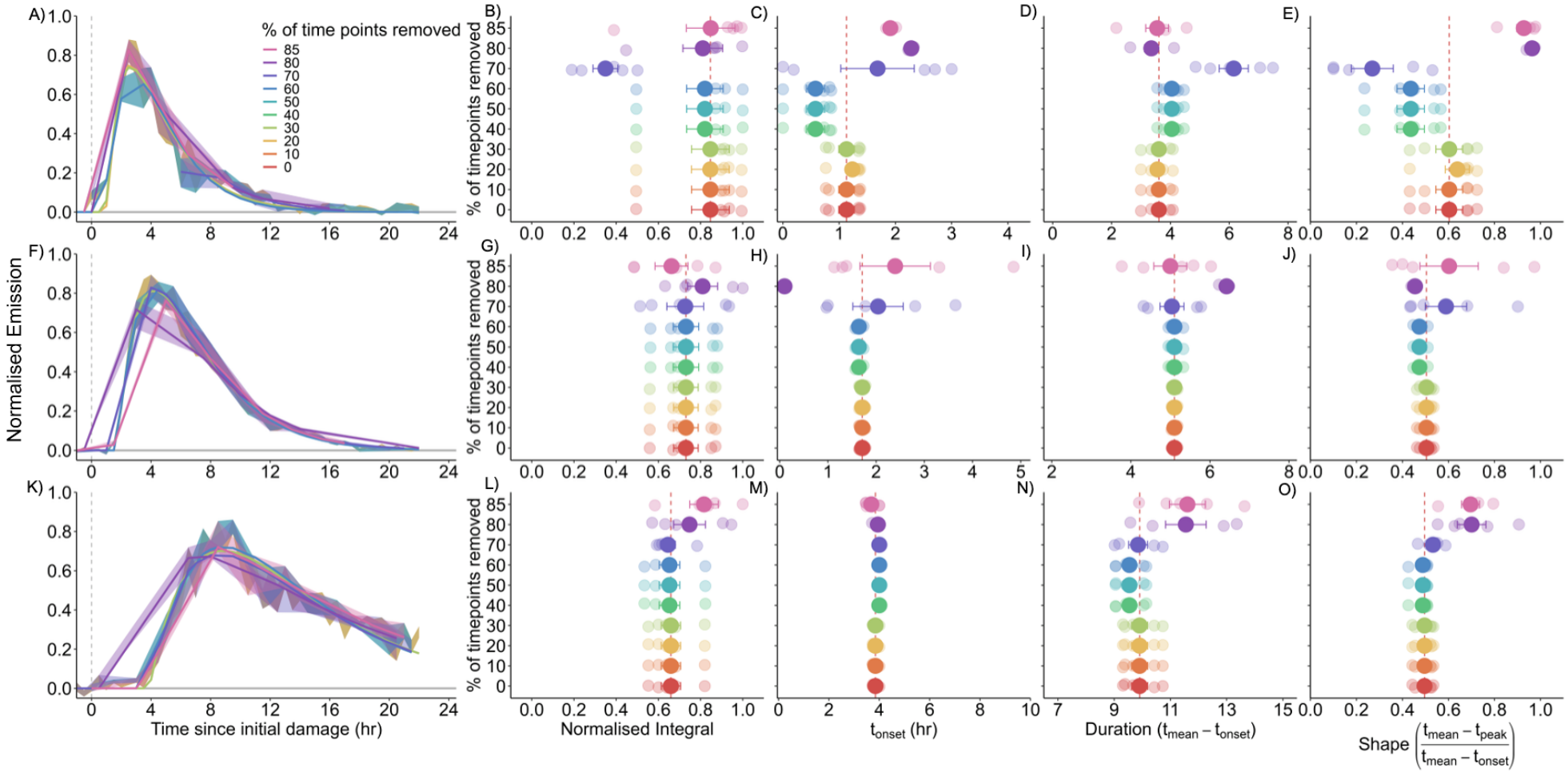

Supplemental Figure 4. Sampling resolution impacts fits. Data were removed systematically in periodic intervals across the entire curve. Emission and fit parameters for A-E) indole, F-J) DMNT and K-O) TMTT. For the first row of data, curves depict emission data, where the solid line represents mean of fitted emission across biological replicates and the translucent ribbon represents the baseline-subtracted raw emission data ± SE. For the remaining columns, solid points represent mean across biological replicates (translucent points). Error bars represent SE. *n* = 5-6. Abbreviations: DMNT= 4,8-dimethylnona-1,3,7-triene, TMTT = 4,8,12-trimethyltrideca-1,3,7,11-tetraene.

332

Discussion

Dynamic responses to environmental stimuli are a universal property of life. Yet, unifying approaches to characterize such responses are lacking. Here, we demonstrate full categorisation and quantification of response features with a relatively simple model and demonstrate its usefulness in revealing new biological patterns. The model improves on traditional response quantification by providing true integrals and maximum response values as well as additional response parameters that are not easily extractable otherwise.

Across biology, we have major gaps in our understanding of patterns and differences in dynamic biological responses. Induced volatile emissions are an illustrative example in this context. In a series of experiments, we find that our model reveals hitherto undocumented differences in volatile induction along circadian, developmental and genetic axes, and in response to wounding and insect-specific molecular patterns. Among the most noteworthy discoveries is that the time of day of wounding has a strong impact on the onset, duration and shape of the volatile induction curve independently of the total response. This provides a window into the tight regulation of the speed and duration of induced volatile emissions by the circadian clock (*10*, *71*), providing new phenotypes that link clock regulation to environmental interactions. Equally noteworthy is the finding that insect oral secretions (OS) enhance differences in response curve shapes between different volatile classes, thus resulting in unique temporal volatile fingerprints. This newly discovered pattern may explain OS-specific responses that affect interactions with herbivores and herbivore natural enemies beyond differences in overall volatile quantities or timing (*72*). Finally, our model uncovers that, contrary to current expectations, the quantity and duration of induced volatile emissions can be regulated independently of each other across plant genotypes. This finding paves the way to identify regulators of volatile induction duration through genetic approaches, potentially leading to the identification of new “late signalling components” involved in sustaining defence

358 responses. Further, these novel dynamic features might ultimately be leveraged to non-
359 destructively distinguish and identify stimuli, for example in an agricultural context, where
360 many individual induced responses may be shared between multiple stressors and total
361 response is thus insufficiently informative (*6*, *45*, *50*).

362 Recent advances in continuous, real-time monitoring have greatly improved our ability to
363 measure biological response dynamics (*5*, *7*, *10*, *50*), yet analyses of such data remain limited.
364 Our modelling approach addresses this gap by providing a standardised framework for
365 quantifying response dynamics in a way that enables biologically and ecologically meaningful
366 comparisons across systems. In this study, we use volatile emissions and gene expression from
367 plants as representative measures of broad biological responses. Thanks to the robustness and
368 generality of the model, it will be straightforward to apply it across biological systems, from
369 energy dynamics in microbes to electron transport in plants to neurological and immune
370 responses in animals (*13*, *17*, *73*, *74*). Thereby, the framework opens opportunities for
371 ambitious endeavours, such as tree-of-life scale meta-analyses, to uncover shared and divergent
372 principles of organismal responses to environmental stimuli and to reveal new fundamental
373 biological phenomena. Furthermore, coupling model parameters with machine-learning
374 algorithms or constrained optimisation solvers could enable the reconstruction of stimulus
375 patterns from observed dynamics, or the prediction of dynamic responses from environmental
376 inputs. We propose this framework as a universal standard for intuitive, interpretable and
377 biologically grounded quantification of dynamic responses, to advance understanding of
378 fundamental processes and to guide innovation across medicine, agriculture and beyond.

379 To ensure that the model can be used widely, we generated a set of freely accessible resources
380 that can be implemented in Python, R and Excel formats (Appendix I), and applied broadly to
381 time-resolved response data to yield all relevant readouts for further statistical analyses.

Materials and Methods

Plants and insects

Plant growth conditions were identical to those used in Waterman et al. (2025). In brief, V2-stage (two developed leaves, one expanding leaf and one emerging leaf) maize (*Zea* mays) seedlings were used throughout the study. At this stage maize plants are particularly susceptible to agricultural pests such as *Spodoptera* spp. (*75*). Plants were grown in commercial potting soil (Selmaterra, BiglerSamen, Switzerland) in 180 mL pots under greenhouse conditions and supplemented with artificial lights (ca. 300 µmol m−2 s−1). The greenhouse was kept at 22 ± 2°C, 40%–60% relative humidity, with a 14 h: 10 h, light: dark cycle.

Spodoptera exigua larvae (Frontier Agricultural Sciences, USA) were reared from eggs on an artificial diet (*76*). At least 24 hr prior to experimental treatments larvae were fed B73 maize leaves. Oral secretions (OS) were collected by probing the mouths of larvae with a pipette tip and stored at -20ºC until use.

Experimental Treatments

All wounds were inflicted using haemostat forceps, an established method of simulating herbivory (*49*, *68*). The maize inbred line, B73, was used unless otherwise stated. The standard damage intensity was 120 mm^2 and time of initial damage was 11:00 unless otherwise stated. To understand how different damage regimes impact induced response dynamics we conducted several experiments spanning a range of treatments:

Variable damage intensity: We damaged plants at 20, 40, 80, 120, 160 and 320 mm^2 on the third-oldest leaf (leaf 3). Damage patterns always encompassed the central segment of each

leaf, and any damage above 40 mm^2 was evenly distributed across the base, middle and tip of leaf 3 (*49*).

Time of day: We damaged plants at 11:00, 11:45, 12:30, 13:15, 14:45, 15:45 and 23:00.

Oral secretions (OS): Damaged plants were either treated with milliQ water or 50% OS from late-instar *Spodoptera exigua* larvae.

Leaf developmental stage: At the V2 stage maize has four leaves: two are fully developed (leaf 1 and leaf 2), one is actively expanding (leaf 3) and one is emerging (leaf 4). We used the raw emission data from Waterman et al. (2025) to measure emission dynamics in each leaf. The damage treatments in the previous study were 60mm^2 total, and damage was inflicted in three bouts of 20 mm^2 damage in *ca.* 30 min intervals

Genotype: To explore the potential variation in response dynamics across maize genotypes we damaged three additional maize inbred lines, with three distinct volatile emission capacities: MO17 (low emission), NC300 (intermediate-high emission) and CML287 (high emission).

Real herbivory: 3rd instar *Spodoptera exigua* were placed on leaf 3 and were left to feed for 30 minutes.

<u>Volatile sampling</u>

Volatiles were collected as in Waterman et al. (2025). Briefly, entire seedlings were placed in transparent glass chambers (Ø×H 12 × 45 cm) that were sealed other than a clean airflow inlet and an outlet. Clean air was supplied at a flow-rate of 0.8 L min^{-1}. Volatiles were measured with a high-throughput platform comprising of a proton transfer reaction time-of-flight mass spectrometer (PTR-ToF-MS; Tofwerk, Switzerland) and a custom-made automated headspace sampling system (Gonin et al. 2018). The outlet of the chamber was accessible to the

427 autosampler/PTR-ToF-MS system, which drew air at 0.1 L min^{-1}. Between samples, a zero-
428 gas measurement was performed for 3 s to flush the system. At each time point (as indicated
429 by the x-axis of the respective figure), volatiles were continuously measured for 25–30 s and
430 averaged to a single mean per sample. Complete mass spectra (0–500 m/z) were recorded in
431 positive mode at *ca*. 10 Hz. The PTR was operated at 100°C and an E/N of approximately 120
432 Td. The volatile data extraction and processing were conducted using Tofware software
433 package v3.2.2 (Tofwerk, Switzerland). Protonated compounds were identified based on their
434 molecular weight + 1. During volatile collection, LED lights (DYNA, heliospectra, Sweden)
435 were placed *ca*. 80 cm above the glass chambers and provided light at 300 µmol m−2 s−1.
436 Identical light:dark cycle timing as in the greenhouse for plant growth was used.

437

438 Gene expression

439 Leaf 3 tissue was harvested 0.5, 1, 1.5, 2, 3 and 5 hr after damage (see above for damage
440 treatment) and flash frozen on liquid nitrogen. Total RNA extraction and purification, genomic
441 DNA removal, cDNA synthesis and quantification of gene expression were conducted
442 identically to Waterman et al. 2024. Quantitative reverse transcription polymerase chain
443 reaction (qRT-PCR) was performed using ORA SEE qPCR Mix (highQu GmbH, Germany) on
444 an Applied Biosystems QuantStudio 5 Real-Time PCR system. The normalized expression
445 (NE) values were calculated as in Waterman et al. (2024) using ubiquitin (UBI1) as the
446 reference gene. Gene identifiers and primer sequences are listed in Table S1.

447

448 Modelling emission dynamics

449 For all experiments, volatile emissions were normalised by the biomass of leaf 3 (damaged
450 leaf). This is because we have previously shown that the size of the damaged leaf is limiting

for volatile emissions (*49*). Additionally, values were normalised to the maximum emission observed in each experiment, yielding a range of positive values < 1.

Choosing the right distribution

To model the waiting time probability distribution, we used a Gamma distribution:

$$f(t;\alpha,\beta) = \frac{t^{\alpha-1}e^{-t/\beta}}{\beta^{\alpha}\Gamma(\alpha)}, \quad t \geq 0$$

Where:

- α is the number of steps,
- β is the rate parameter (for each step),
- $\Gamma(\alpha)$ is the Gamma function evaluated at α

This distribution arises from the sum of several exponential waiting times, making it suited to processes where multiple sequential steps precede a single observable outcome (*77*). Unlike the log-normal or inverse Gaussian, the Gamma distribution is closed under addition, meaning that the sum of sequential Gamma is itself a Gamma distribution (*78*). This allows modelling of both early and late phase responses, even if they are both part of the same chain of events. In the formal definition, α represents the effective number of steps and β an effective average delay, though we do not assume that these biological processes are truly memoryless and independent as required by the strict derivation. Instead, we treat the Gamma distribution as a phenomenological approximation of the process, which fits the shapes of the responses we (and others) observe well (*1*, *2*, *28*, *49–57*). With this in mind, we make a number of meaningful reparameterisations to the standard Gamma distribution, as follows.

We begin with the standard Gamma distribution and introduce a shifted time variable t_{adj} to account for a delay in the onset of the curve:

$$t_{adj} = t - t_{onset}.$$

The Gamma probability density function is then given by:

$$f(t; \alpha, \beta, t_{onset}) = \frac{t_{adj}^{\alpha-1} e^{-t_{adj}/\beta}}{\beta^{\alpha}\Gamma(\alpha)}, \quad t \geq t_{onset}.$$

Our next step is to relate the variables to observable quantities, and so we want to express α and β in terms of measurable features of the response curve.

For the Gamma distribution:

- $Mode = (\alpha - 1)\beta = t_{peak} - t_{onset}$

representing the time at which the response reaches its peak.

- $Mean = \alpha\beta = t_{mean} - t_{onset}$

representing the average time after onset that the response occurs.

In order to solve for α and β for these observable features we:

Subtract the first from the second:

$$Mode - Mean = \alpha\beta - (\alpha - 1)\beta = (t_{mean} - t_{onset}) - \left(t_{peak} - t_{onset}\right).$$

Simplify:

$$\beta = t_{mean} - t_{peak}.$$

Substitute into $\alpha\beta = t_{mean} - t_{onset}$:

$$\alpha = \frac{t_{mean} - t_{onset}}{\beta} = \frac{t_{mean} - t_{onset}}{t_{mean} - t_{peak}}.$$

The Gamma probability density function is normalised to integrate to 1.

However, in experimental data the absolute amplitude (the response intensity, R_{peak}) is an observable quantity and so we define the response model:

$$R(t) = R_{peak} \cdot \frac{f(t;\alpha,\beta,t_{onset})}{f(t_{peak};\alpha,\beta,t_{onset})},$$

where R_{peak} is the observed response at t_{peak}.

This ensures that the curve shape follows the Gamma form, and that the maximum of $R(t)$ equals R_{peak}.

The next step is to solve for $f(t_{peak}; \alpha, \beta, t_{onset})$

Substitute $t = t_{peak}$ into $f(t; \alpha, \beta, t_{onset})$:

$$f(t_{\text{peak}}; \alpha, \beta, t_{\text{onset}}) = \frac{(t_{\text{peak}} - t_{\text{onset}})^{\alpha-1} \exp\left(-\frac{t_{\text{peak}} - t_{\text{onset}}}{\beta}\right)}{\beta^{\alpha}\Gamma(\alpha)}.$$

Replace $t_{peak} - t_{onset}$ with $(\alpha - 1)\beta$ using the mode definition:

$$f(t_{\text{peak}}; \alpha, \beta, t_{\text{onset}}) = \frac{[(\alpha - 1)\beta]^{\alpha-1}\, exp^{\left(-\frac{(\alpha-1)\beta}{\beta}\right)}}{\beta^{\alpha}\,\Gamma(\alpha)}.$$

Simplify the exponent:

$$\exp\left(-\frac{(\alpha-1)\beta}{\beta}\right) = e^{-(\alpha-1)}.$$

Final expression:

$$f\left(t_{peak};\alpha,\beta,t_{onset}\right) = \frac{[(\alpha-1)\beta]^{\alpha-1}e^{-(\alpha-1)}}{\beta^{\alpha}\Gamma(\alpha)}.$$

We can therefore define:

$$R_{peak} = f\left(t_{peak};\alpha,\beta,t_{onset}\right) = \frac{[(\alpha-1)\beta]^{\alpha-1}e^{-(\alpha-1)}}{\beta^{\alpha}\Gamma(\alpha)}.$$

Substituting back to obtain the final model:

Substitute $f(t)$and $f\left(t_{peak}\right)$ into the ratio:

$$R(t) = R_{\text{peak}} \cdot \frac{\dfrac{(t-t_{\text{onset}})^{\alpha-1}\exp\left(-\dfrac{t-t_{\text{onset}}}{\beta}\right)}{\beta^{\alpha}\Gamma(\alpha)}}{\dfrac{\left(t_{\text{peak}}-t_{\text{onset}}\right)^{\alpha-1}\exp\left(-\dfrac{t_{\text{peak}}-t_{\text{onset}}}{\beta}\right)}{\beta^{\alpha}\Gamma(\alpha)}}$$

Cancel the common terms $\beta^{\alpha}\Gamma(\alpha)$:

$$R(t) = R_{\text{peak}} \cdot \left(\frac{t-t_{\text{onset}}}{t_{\text{peak}}-t_{\text{onset}}}\right)^{\alpha-1} \cdot \exp\left(-\frac{(t-t_{\text{onset}})-\left(t_{\text{peak}}-t_{\text{onset}}\right)}{\beta}\right)$$

Simplify the exponent:

$$R(t) = R_{peak} \cdot \left(\frac{t-t_{onset}}{t_{peak}-t_{onset}}\right)^{\alpha-1} \cdot \exp\left(-\frac{t-t_{peak}}{\beta}\right)$$

Replace α and β with expressions in terms of $(t_{onset}, t_{peak}, t_{mean})$ to give the final model:

$$R(t) = R_{\text{peak}} \cdot \left(\frac{t - t_{\text{onset}}}{t_{\text{peak}} - t_{\text{onset}}}\right)^{\frac{t_{\text{mean}} - t_{\text{onset}}}{t_{\text{mean}} - t_{\text{peak}}} - 1} \cdot \exp\left(-\frac{t - t_{\text{peak}}}{t_{\text{mean}} - t_{\text{peak}}}\right)$$

Where:

- R_{peak} is the maximum measured response,
- t_{onset} is the onset delay,
- t_{peak} is the time of peak response,
- t_{mean} is the mean response time.

Background subtraction

Since low levels of plant volatiles are constantly emitted even without wounding or other measurable stimuli, a background curve was subtracted so that only induced emissions were modelled (*42*). This background was estimated from undamaged plants and either directly subtracted or scaled to the pre-damage baseline to correct for instrumental drift or individual plant batch variation.

Fitting

Each individual curve was fit using a two-stage optimisation approach. In order to avoid local minima, we first used a differential evolution optimisation followed by a local refinement step using SLSQP (*79*). Since the emission data were individually relatively noisy, we reconstructed the dominant temporal trend using singular value decomposition (SVD) and incorporated this as a weak prior to guide the fitting algorithm toward biologically realistic solutions (*80*, *81*).

A number of constraints and bounds were enforced in order to guide the fitting of the data. Temporal ordering was imposed such that $t_{onset} < t_{peak} < t_{mean}$. To prevent degenerate solutions, minimum separations were required, with $t_{peak} - t_{onset} > 0.1$ and $t_{mean} - t_{peak} > 0.1$. Bounds were also dynamically set for each curve; for instance, t_{peak} was initialised at the time of maximum observed response and restricted to within ±20% of this value, while R_{peak} was constrained between 80% and 120% of the observed maximum. t_{onset} and t_{mean} times were shifted according to experimental timing and constrained within empirically informed ranges. All fitting, calculations and data manipulation were done using SciPy (*60*), NumPy (*82*) and Pandas (*83*) in Python 3.12.4 (*84*).

Model testing

To explore the robustness of the model and fitting methods to the effects of resolution and measurement time, a data set was taken and data were removed in order to simulate a lower quality measurement. We chose the dataset of damage plants treated with insect OS, as a representative and ecologically relevant subset. In a first test, data from the end of the measurement were removed in a stepwise manner to simulate a shorter (incomplete) experimental measurement period. Secondly, data were systematically down-sampled to simulate a lower resolution measurement. After each step of the truncation or down sampling the data was fit and the fit parameters compared.

<u>Additional statistical analyses</u>

All further statistical analyses were conducted in R version 4.4.2 (*85*). Differences in model outputs between groups were determined using one-way ANOVA. Where necessary, data were

transformed to meet ANOVA assumptions. Where necessary, to obtain heteroscedasticity-consistent standard errors, White-adjusted ANOVAs were used (*86*). Where data did not meet the assumptions of ANOVA, even following transformation, differences were determined using a Kruskal–Wallis test. Statistical test summaries are included in supplemental tables 1-4.

References

1. M. Erb, N. Veyrat, C. A. M. Robert, H. Xu, M. Frey, J. Ton, T. C. J. Turlings, Indole is an essential herbivore-induced volatile priming signal in maize. *Nature Communications* **6**, 6273 (2015).

2. Y.-Q. Gao, P. Jimenez-Sandoval, S. Tiwari, S. Stolz, J. Wang, G. Glauser, J. Santiago, E. E. Farmer, Ricca's factors as mobile proteinaceous effectors of electrical signaling. *Cell* **186**, 1337-1351.e20 (2023).

3. H. P. Lu, L. Xun, X. S. Xie, Single-Molecule Enzymatic Dynamics. *Science* **282**, 1877–1882 (1998).

4. M. Toyota, D. Spencer, S. Sawai-Toyota, W. Jiaqi, T. Zhang, A. J. Koo, G. A. Howe, S. Gilroy, Glutamate triggers long-distance, calcium-based plant defense signaling. *Science* **361**, 1112–1115 (2018).

5. L. Yang, V. Pathiranage, S. Zhou, X. Sun, H. Zhang, C. Lai, C. Gu, F. V. Subach, M. Drobizhev, A. R. Walker, K. D. Piatkevich, Sensitive red fluorescent indicators for real-time visualization of potassium ion dynamics in vivo. *PLOS Biology* **23**, e3002993 (2025).

6. M. C.-Y. Ang, J. M. Saju, T. K. Porter, S. Mohaideen, S. Sarangapani, D. T. Khong, S. Wang, J. Cui, S. I. Loh, G. P. Singh, N.-H. Chua, M. S. Strano, R. Sarojam, Decoding early stress signaling waves in living plants using nanosensor multiplexing. *Nature Communications* **15**, 2943 (2024).

7. P. Coatsworth, L. Gonzalez-Macia, A. S. P. Collins, T. Bozkurt, F. Güder, Continuous monitoring of chemical signals in plants under stress. *Nature Reviews Chemistry* **7**, 7–25 (2023).

8. R. Grote, M. Sharma, A. Ghirardo, J.-P. Schnitzler, A New Modeling Approach for Estimating Abiotic and Biotic Stress-Induced de novo Emissions of Biogenic Volatile Organic Compounds From Plants. *Frontiers in Forests and Global Change* **Volume 2-2019** (2019).

9. L. Oyarte Galvez, C. Bisot, P. Bourrianne, R. Cargill, M. Klein, M. van Son, J. van Krugten, V. Caldas, T. Clerc, K.-K. Lin, F. Kahane, S. van Staalduine, J. D. Stewart, V. Terry, B. Turcu, S. van Otterdijk, A. Babu, M. Kamp, M. Seynen, B. Steenbeek, J.

Zomerdijk, E. Tutucci, M. Sheldrake, C. Godin, V. Kokkoris, H. A. Stone, E. T. Kiers, T. S. Shimizu, A travelling-wave strategy for plant–fungal trade. *Nature* **639**, 172–180 (2025).

10. J. M. Waterman, T. M. Cofer, L. Wang, G. Glauser, M. Erb, High-resolution kinetics of herbivore-induced plant volatile transfer reveal clocked response patterns in neighboring plants. *eLife* **12**, RP89855 (2024).

11. J. Zhang, H. Yin, J. Zhang, G. Yang, J. Qin, L. He, Real-time mental stress detection using multimodality expressions with a deep learning framework. *Frontiers in Neuroscience* **Volume 16-2022** (2022).

12. Ü. Niinemets, A. Kännaste, L. Copolovici, Quantitative patterns between plant volatile emissions induced by biotic stresses and the degree of damage. *Frontiers in Plant Science* **Volume 4-2013** (2013).

13. J. Reyes-Silveyra, A. R. Mikler, Modeling immune response and its effect on infectious disease outbreak dynamics. *Theoretical Biology and Medical Modelling* **13**, 10 (2016).

14. V. S. Pan, E. Ghosh, P. J. Ode, W. C. Wetzel, K. J. Gilbert, I. S. Pearse, Large Differences in Herbivore Performance Emerge From Simple Herbivore Behaviours and Fine-Scale Spatial Heterogeneity in Phytochemistry. *Ecology Letters* **28**, e70044 (2025).

15. I. S. Pearse, R. Paul, P. J. Ode, Variation in Plant Defense Suppresses Herbivore Performance. *Current Biology* **28**, 1981-1986.e2 (2018).

16. W. C. Wetzel, H. M. Kharouba, M. Robinson, M. Holyoak, R. Karban, Variability in plant nutrients reduces insect herbivore performance. *Nature* **539**, 425–427 (2016).

17. T. Branco, B. A. Clark, M. Häusser, Dendritic Discrimination of Temporal Input Sequences in Cortical Neurons. *Science* **329**, 1671–1675 (2010).

18. B. Grothe, M. Pecka, D. McAlpine, Mechanisms of Sound Localization in Mammals. *Physiological Reviews* **90**, 983–1012 (2010).

19. J. M. Köhler, Vaccination, Immunity and Breakthrough: Quantitative Effects in Individual Immune Responses Illustrated by a Simple Kinetic Model. *Applied Sciences* **12** (2022).

20. P. A. Gagliardi, O. Pertz, The mitogen-activated protein kinase network, wired to dynamically function at multiple scales. *Current Opinion in Cell Biology* **88**, 102368 (2024).

21. I. Kinjyo, J. Qin, S.-Y. Tan, C. J. Wellard, P. Mrass, W. Ritchie, A. Doi, L. L. Cavanagh, M. Tomura, A. Sakaue-Sawano, O. Kanagawa, A. Miyawaki, P. D. Hodgkin, W. Weninger, Real-time tracking of cell cycle progression during CD8+ effector and memory T-cell differentiation. *Nature Communications* **6**, 6301 (2015).

22. A. Stirbet, D. Lazár, Y. Guo, G. Govindjee, Photosynthesis: basics, history and modelling. *Annals of Botany* **126**, 511–537 (2020).

23. J. WU, I. T. BALDWIN, Herbivory-induced signalling in plants: perception and action. *Plant, Cell & Environment* **32**, 1161–1174 (2009).

24. X. Yu, B. Feng, P. He, L. Shan, From Chaos to Harmony: Responses and Signaling upon Microbial Pattern Recognition, *Annual Review of Phytopathology*. **55** (2017)pp. 109–137.

25. J. M. S. Zegers, I. Irisarri, S. de Vries, J. de Vries, Evolving circuitries in plant signaling cascades. *Journal of Cell Science* **137**, jcs261712 (2024).

26. A. K. Block, C. T. Hunter, C. Rering, S. A. Christensen, R. L. Meagher, Contrasting insect attraction and herbivore-induced plant volatile production in maize. *Planta* **248**, 105–116 (2018).

27. R. Moreno-Sánchez, E. Saavedra, S. Rodríguez-Enríquez, V. Olín-Sandoval, Metabolic Control Analysis: A Tool for Designing Strategies to Manipulate Metabolic Pathways. *BioMed Research International* **2008**, 597913 (2008).

28. S. A. R. Mousavi, A. Chauvin, F. Pascaud, S. Kellenberger, E. E. Farmer, GLUTAMATE RECEPTOR-LIKE genes mediate leaf-to-leaf wound signalling. *Nature* **500**, 422–426 (2013).

29. Y. Blum, J. Mikelson, M. Dobrzyński, H. Ryu, M. Jacques, N. L. Jeon, M. Khammash, O. Pertz, Temporal perturbation of ERK dynamics reveals network architecture of FGF2/MAPK signaling. *Molecular Systems Biology* **15**, e8947 (2019).

30. C. Dessauges, J. Mikelson, M. Dobrzyński, M. Jacques, A. Frismantiene, P. A. Gagliardi, M. Khammash, O. Pertz, Optogenetic actuator – ERK biosensor circuits identify MAPK network nodes that shape ERK dynamics. *Molecular Systems Biology* **18**, e10670 (2022).

31. T. K. Porter, M. N. Heinz, D. J. Lundberg, A. M. Brooks, T. T. S. Lew, K. S. Silmore, V. B. Koman, M. C.-Y. Ang, D. T. Khong, G. P. Singh, J. W. Swan, R. Sarojam, N.-H. Chua, M. S. Strano, A theory of mechanical stress-induced H2O2 signaling waveforms in Planta. *Journal of Mathematical Biology* **86**, 11 (2022).

32. T. K. Porter, G. Sánchez-Velázquez, M. S. Strano, The Role of Basal H2O2 Concentration in ROS Stress Signaling Waveforms In Planta. *ACS Agric. Sci. Technol.* **5**, 1434–1441 (2025).

33. P. A. Saa, L. K. Nielsen, Construction of feasible and accurate kinetic models of metabolism: A Bayesian approach. *Scientific Reports* **6**, 29635 (2016).

34. L. M. Tran, M. L. Rizk, J. C. Liao, Ensemble Modeling of Metabolic Networks. *Biophysical Journal* **95**, 5606–5617 (2008).

35. A. Khodayari, C. D. Maranas, A genome-scale Escherichia coli kinetic metabolic model k-ecoli457 satisfying flux data for multiple mutant strains. *Nature Communications* **7**, 13806 (2016).

36. H. Link, D. Christodoulou, U. Sauer, Advancing metabolic models with kinetic information. *Current Opinion in Biotechnology* **29**, 8–14 (2014).

37. R. N. Gutenkunst, J. J. Waterfall, F. P. Casey, K. S. Brown, C. R. Myers, J. P. Sethna, Universally Sloppy Parameter Sensitivities in Systems Biology Models. *PLOS Computational Biology* **3**, e189 (2007).

38. M. E. Bergman, R. W. J. Kortbeek, M. Gutensohn, N. Dudareva, Plant terpenoid biosynthetic network and its multiple layers of regulation. *Progress in Lipid Research* **95**, 101287 (2024).

39. J.-K. Weng, The evolutionary paths towards complexity: a metabolic perspective. *New Phytologist* **201**, 1141–1149 (2014).

40. J. P. Torres, Z. Lin, J. M. Winter, P. J. Krug, E. W. Schmidt, Animal biosynthesis of complex polyketides in a photosynthetic partnership. *Nature Communications* **11**, 2882 (2020).

41. M. E. De Obaldia, T. Morita, L. C. Dedmon, D. J. Boehmler, C. S. Jiang, E. V. Zeledon, J. R. Cross, L. B. Vosshall, Differential mosquito attraction to humans is associated with skin-derived carboxylic acid levels. *Cell* **185**, 4099-4116.e13 (2022).

42. R. Escobar-Bravo, P.-A. Lin, J. M. Waterman, M. Erb, Dynamic environmental interactions shaped by vegetative plant volatiles. *Nat. Prod. Rep.* **40**, 840–865 (2023).

43. A. M. Angioy, A. Desogus, I. T. Barbarossa, P. Anderson, B. S. Hansson, Extreme Sensitivity in an Olfactory System. *Chemical Senses* **28**, 279–284 (2003).

44. H. Guo, D. P. Smith, Time-Dependent Odorant Sensitivity Modulation in Insects. *Insects* **13** (2022).

45. P. Zu, K. Boege, E. del-Val, M. C. Schuman, P. C. Stevenson, A. Zaldivar-Riverón, S. Saavedra, Information arms race explains plant-herbivore chemical communication in ecological communities. *Science* **368**, 1377–1381 (2020).

46. Y. Qin, L. Wang, D. Zhong, Dynamics and mechanism of ultrafast water–protein interactions. *Proceedings of the National Academy of Sciences* **113**, 8424–8429 (2016).

47. M. Shibata, H. Nishimasu, N. Kodera, S. Hirano, T. Ando, T. Uchihashi, O. Nureki, Real-space and real-time dynamics of CRISPR-Cas9 visualized by high-speed atomic force microscopy. *Nature Communications* **8**, 1430 (2017).

48. E. T. Wurtzel, T. M. Kutchan, Plant metabolism, the diverse chemistry set of the future. *Science* **353**, 1232–1236 (2016).

49. J. M. Waterman, T. M. Cofer, O. M. Von Laue, P. Mateo, L. Wang, M. Erb, Leaf Size Determines Damage- and Herbivore-Induced Volatile Emissions in Maize. *Plant, Cell & Environment* **10.1111/pce.15355** (2025).

50. T. T. S. Lew, V. B. Koman, K. S. Silmore, J. S. Seo, P. Gordiichuk, S.-Y. Kwak, M. Park, M. C.-Y. Ang, D. T. Khong, M. A. Lee, M. B. Chan-Park, N.-H. Chua, M. S. Strano, Real-time detection of wound-induced H2O2 signalling waves in plants with optical nanosensors. *Nature Plants* **6**, 404–415 (2020).

51. A. D. Steinbrenner, M. Muñoz-Amatriaín, A. F. Chaparro, J. M. Aguilar-Venegas, S. Lo, S. Okuda, G. Glauser, J. Dongiovanni, D. Shi, M. Hall, D. Crubaugh, N. Holton, C. Zipfel, R. Abagyan, T. C. J. Turlings, T. J. Close, A. Huffaker, E. A. Schmelz, A receptor-like protein mediates plant immune responses to herbivore-associated molecular patterns. *Proceedings of the National Academy of Sciences* **117**, 31510–31518 (2020).

52. L. Wang, E. Einig, M. Almeida-Trapp, M. Albert, J. Fliegmann, A. Mithöfer, H. Kalbacher, G. Felix, The systemin receptor SYR1 enhances resistance of tomato against herbivorous insects. *Nature Plants* **4**, 152–156 (2018).

53. J. M. Waterman, C. R. Hall, M. Mikhael, C. I. Cazzonelli, S. E. Hartley, S. N. Johnson, Short-term resistance that persists: Rapidly induced silicon anti-herbivore defence affects carbon-based plant defences. *Functional Ecology* **35**, 82–92 (2021).

54. K. C. Sridhar, N. Hersch, G. Dreissen, R. Merkel, B. Hoffmann, Calcium mediated functional interplay between myocardial cells upon laser-induced single-cell injury: an in vitro study of cardiac cell death signaling mechanisms. *Cell Communication and Signaling* **18**, 191 (2020).

55. X. Wang, H. Fang, Z. Huang, W. Shang, T. Hou, A. Cheng, H. Cheng, Imaging ROS signaling in cells and animals. *Journal of Molecular Medicine* **91**, 917–927 (2013).

56. T.-O. Kiess, J. Kockskämper, SERCA Activity Controls the Systolic Calcium Increase in the Nucleus of Cardiac Myocytes. *Frontiers in Physiology* **Volume 10-2019** (2019).

57. R. Vosoughi, Z. Sadeghi Goghari, A. H. Jafari, Modelling system of two insulin-glucose delays to achieve the dynamics of glucose changes. *Journal of Biomedical Physics and Engineering* **12**, 189–204 (2022).

58. D. Morris, J. Maclean, A. J. Black, Computation of random time-shift distributions for stochastic population models. *Journal of Mathematical Biology* **89**, 33 (2024).

59. Y. Jiang, J. Ye, B. Rasulov, Ü. Niinemets, Role of Stomatal Conductance in Modifying the Dose Response of Stress-Volatile Emissions in Methyl Jasmonate Treated Leaves of Cucumber (Cucumis Sativa). *International Journal of Molecular Sciences* **21** (2020).

60. P. Virtanen, R. Gommers, T. E. Oliphant, M. Haberland, T. Reddy, D. Cournapeau, E. Burovski, P. Peterson, W. Weckesser, J. Bright, S. J. van der Walt, M. Brett, J. Wilson, K. J. Millman, N. Mayorov, A. R. J. Nelson, E. Jones, R. Kern, E. Larson, C. J. Carey, İ. Polat, Y. Feng, E. W. Moore, J. VanderPlas, D. Laxalde, J. Perktold, R. Cimrman, I. Henriksen, E. A. Quintero, C. R. Harris, A. M. Archibald, A. H. Ribeiro, F. Pedregosa, P. van Mulbregt, A. Vijaykumar, A. P. Bardelli, A. Rothberg, A. Hilboll, A. Kloeckner, A. Scopatz, A. Lee, A. Rokem, C. N. Woods, C. Fulton, C. Masson, C. Häggström, C. Fitzgerald, D. A. Nicholson, D. R. Hagen, D. V. Pasechnik, E. Olivetti, E. Martin, E. Wieser, F. Silva, F. Lenders, F. Wilhelm, G. Young, G. A. Price, G.-L. Ingold, G. E. Allen, G. R. Lee, H. Audren, I. Probst, J. P. Dietrich, J. Silterra, J. T. Webber, J. Slavič, J. Nothman, J. Buchner, J. Kulick, J. L. Schönberger, J. V. de Miranda Cardoso, J. Reimer, J. Harrington, J. L. C. Rodríguez, J. Nunez-Iglesias, J. Kuczynski, K. Tritz, M. Thoma, M. Newville, M. Kümmerer, M. Bolingbroke, M. Tartre, M. Pak, N. J. Smith, N. Nowaczyk, N. Shebanov, O. Pavlyk, P. A. Brodtkorb, P. Lee, R. T. McGibbon, R.

Feldbauer, S. Lewis, S. Tygier, S. Sievert, S. Vigna, S. Peterson, S. More, T. Pudlik, T. Oshima, T. J. Pingel, T. P. Robitaille, T. Spura, T. R. Jones, T. Cera, T. Leslie, T. Zito, T. Krauss, U. Upadhyay, Y. O. Halchenko, Y. Vázquez-Baeza, SciPy 1.0 Contributors, SciPy 1.0: fundamental algorithms for scientific computing in Python. *Nature Methods* **17**, 261–272 (2020).

61. M. Abramowitz, Stegun, I.A., *Handbook of Mathematical Functions with Formulas, Graphs and Mathematical Tables* (Dover, New York, ed. 9).

62. A. LoPrete, J. Burge, Bandwidth of Gamma-Distribution-Shaped Functions via Lambert W Function (2025). https://arxiv.org/abs/2509.19307.

63. C. Chen, H. Chen, S. Huang, T. Jiang, C. Wang, Z. Tao, C. He, Q. Tang, P. Li, Volatile DMNT directly protects plants against Plutella xylostella by disrupting the peritrophic matrix barrier in insect midgut. *eLife* **10**, e63938 (2021).

64. G. M. Gurr, J. Liu, J. A. Pickett, P. C. Stevenson, Review of the chemical ecology of homoterpenes in arthropod–plant interactions. *Austral Entomology* **62**, 3–14 (2023).

65. E. Hatano, A. M. Saveer, F. Borrero-Echeverry, M. Strauch, A. Zakir, M. Bengtsson, R. Ignell, P. Anderson, P. G. Becher, P. Witzgall, T. Dekker, A herbivore-induced plant volatile interferes with host plant and mate location in moths through suppression of olfactory signalling pathways. *BMC Biology* **13**, 75 (2015).

66. J. Hua, Modulation of plant immunity by light, circadian rhythm, and temperature. *Current Opinion in Plant Biology* **16**, 406–413 (2013).

67. N. Guayazán Palacios, T. Imaizumi, A. D. Steinbrenner, The Circadian Clock Regulates Receptor-Mediated Immune Responses to a Herbivore-Associated Molecular Pattern. *Plant, Cell & Environment* **n/a** (2025).

68. J. M. Waterman, C. I. Cazzonelli, S. E. Hartley, S. N. Johnson, Simulated Herbivory: The Key to Disentangling Plant Defence Responses. *Trends in Ecology & Evolution* **34**, 447–458 (2019).

69. T. Degen, C. Dillmann, F. Marion-Poll, T. C. J. Turlings, High Genetic Variability of Herbivore-Induced Volatile Emission within a Broad Range of Maize Inbred Lines. *Plant Physiology* **135**, 1928–1938 (2004).

70. P.-A. Lin, Y. Chen, D. Chaverra-Rodriguez, C. C. Heu, N. B. Zainuddin, J. S. Sidhu, M. Peiffer, C.-W. Tan, A. Helms, D. Kim, J. Ali, J. L. Rasgon, J. Lynch, C. T. Anderson, G. W. Felton, Silencing the alarm: an insect salivary enzyme closes plant stomata and inhibits volatile release. *New Phytologist* **230**, 793–803 (2021).

71. Y. Joo, J. K. Goldberg, L. T. S. Chrétien, S.-G. Kim, I. T. Baldwin, M. C. Schuman, The circadian clock contributes to diurnal patterns of plant indirect defense in nature. *Journal of Integrative Plant Biology* **61**, 924–928 (2019).

72. N. G. Palacios, P. Grof-Tisza, B. Behnken, C. M. Arce, D. Wu, A. F. Chaparro, E. A. Schmelz, T. C. J. Turlings, B. Benrey, A. D. Steinbrenner, A plant immune receptor mediates tritrophic interactions by linking caterpillar detection to predator recruitment. *bioRxiv*, 2025.07.29.667524 (2025).

73. X. Mu, T. D. Evans, F. Zhang, ATP biosensor reveals microbial energetic dynamics and facilitates bioproduction. *Nature Communications* **15**, 5299 (2024).

74. C. Chondrogiannis, G. Grammatikopoulos, Transition from juvenility to maturity strengthens photosynthesis in sclerophyllous and deciduous but not in semi-deciduous Mediterranean shrubs. *Environmental and Experimental Botany* **181**, 104265 (2021).

75. J. van den Berg, C. Britz, H. du Plessis, Maize Yield Response to Chemical Control of Spodoptera frugiperda at Different Plant Growth Stages in South Africa. *Agriculture* **11** (2021).

76. D. Maag, C. Dalvit, D. Thevenet, A. Köhler, F. C. Wouters, D. G. Vassão, J. Gershenzon, J.-L. Wolfender, T. C. J. Turlings, M. Erb, G. Glauser, 3-β-d-Glucopyranosyl-6-methoxy-2-benzoxazolinone (MBOA-N-Glc) is an insect detoxification product of maize 1,4-benzoxazin-3-ones. *Phytochemistry* **102**, 97–105 (2014).

77. W. Feller, *An Introduction to Probability Theory and Its Applications* (Wiley, ed. 2, 1971)vol. 2.

78. N. L. Johnson, S. Kotz, N. Balakrishnan, *Continuous Univariate Distributions* (Wiley, ed. 2, 1994)vol. 1.

79. D. Kraft, *A Software Package for Sequential Quadratic Programming* (Wiss. Berichtswesen d. DFVLR, 1988; https://books.google.ie/books?id=4rKaGwAACAAJ)*Deutsche Forschungs- und Versuchsanstalt für Luft- und Raumfahrt Köln: Forschungsbericht*.

80. A. Gelman, J. B. Carlin, H. S. Stern, D. B. Dunson, A. Vehtari, D. B. Rubin, *Bayesian Data Analysis* (CRC Press, 2013; https://books.google.ie/books?id=eSHSBQAAQBAJ)*Chapman & Hall/CRC Texts in Statistical Science*.

81. G. H. Golub, C. Reinsch, Singular value decomposition and least squares solutions. *Numerische Mathematik* **14**, 403–420 (1970).

82. C. R. Harris, K. J. Millman, S. J. van der Walt, R. Gommers, P. Virtanen, D. Cournapeau, E. Wieser, J. Taylor, S. Berg, N. J. Smith, R. Kern, M. Picus, S. Hoyer, M. H. van Kerkwijk, M. Brett, A. Haldane, J. F. del Río, M. Wiebe, P. Peterson, P. Gérard-Marchant, K. Sheppard, T. Reddy, W. Weckesser, H. Abbasi, C. Gohlke, T. E. Oliphant, Array programming with NumPy. *Nature* **585**, 357–362 (2020).

83. The Pandas Development Team, pandas-dev/pandas: Pandas, version v2.2.2, Zenodo (2024); https://doi.org/10.5281/zenodo.10957263.

84. G. Van Rossum, F. L. Drake, *Python 3 Reference Manual* (CreateSpace, Scotts Valley, CA, 2009).

85. R Core Team, R: A Language and Environment for Statistical Computing., version 4.4.2, R Foundation for Statistical Computing (2024); https://www.R-project.org/.

86. H. White, A Heteroskedasticity-Consistent Covariance Matrix Estimator and a Direct Test for Heteroskedasticity. *Econometrica* **48**, 817–838 (1980).

Funding

This work was supported by the Swiss National Science Foundation (Grant Nr. 201651), the State Secretariat for Education, Research and Innovation (CANWAS), Trinity College Dublin and the University of Bern.

Author contributions

Conceptualization: JMW, GM, LAC, ME

Methodology: JMW, GM, LAC, ME

Investigation: JMW, GM, LAC, SH, ME

Visualization: JMW, GM

Funding acquisition: JMW, ME

Project administration: JMW, ME

Writing (all drafts): JMW, GM, LAC, ME

Competing Interests

The authors have no competing interests to declare.

Data and Materials Availability

All data and code are available upon request from the authors. Additionally, we provide examples of how to adopt the presented approach in Python, R and Excel formats (see Appendix I).

Supplemental Tables

Supplemental Table 1. Summary of statistical analyses presented in Figure 2 (main text). Bold values: $p < 0.05$. a = analysed using one-way ANOVA, b = analysed using a Kruskal-Wallis test, * = analysed on log-transformed data, † = analysed using white-adjusted ANOVAs.

Response	F/χ^2	*p-value*	*df*
Damage Intensity			
$Integral^{*a}$	**13.10**	**< 0.001**	**5**
$t_{onset}{}^{a}$	0.37	0.863	5
$Duration^{a}$	**4.69**	**0.004**	**5**
$Shape^{a}$	2.00	0.115	5
Circadian clock			
$Integral^{*a}$	0.502	0.772	5
$t_{onset}{}^{a}$	**14.77**	**< 0.001**	**5**
$Duration^{b}$	**24.42**	**< 0.001**	**5**
$Shape^{*a}$	**11.70**	**< 0.001**	**5**
Oral secretions			
$Integral^{a}$	**22.84**	**0.001**	**1**
$t_{onset}{}^{a}$	**7.49**	**0.026**	**1**
$Duration^{a}$	**94.53**	**< 0.001**	**1**
$Shape^{a}$	**19.53**	**0.002**	**1**
Leaf number			
$Integral^{a}$	**9.18**	**0.004**	**2**
$t_{onset}{}^{\dagger a}$	0.47	0.636	2
$Duration^{a}$	**235.36**	**< 0.001**	**2**
$Shape^{a}$	**126.62**	**< 0.001**	**2**
Genotype			
$Integral^{\dagger a}$	**46.98**	**< 0.001**	**2**
$t_{onset}{}^{a}$	**115.36**	**< 0.001**	**2**
$Duration^{a}$	**94.85**	**< 0.001**	**2**
$Shape^{*a}$	**58.92**	**< 0.001**	**2**

Supplemental Figure 2. Summary of statistical analyses presented in Figure 3 (main text). Bold values: $p < 0.05$. a = analysed using one-way ANOVA, b = analysed using a Kruskal-Wallis test, * = analysed on log-transformed data, † = analysed using white-adjusted ANOVAs, ‡ = analysed on square-root-transformed data.

Response	F/χ^2	*p-value*	*df*
Without oral secretions			
$Integral^{\dagger a}$	1.69	0.19	4
$t_{onset}{}^{\ddagger a}$	**39.78**	**< 0.001**	**4**
$Duration^{a}$	**95.42**	**< 0.001**	**4**
$Shape^{*a}$	**34.31**	**< 0.001**	**4**
With oral secretions			
$Integral^{a}$	**6.12**	**0.002**	**4**
$t_{onset}{}^{*a}$	**1416.00**	**< 0.001**	**4**
$Duration^{\dagger a}$	**274.58**	**< 0.001**	**4**
$Shape^{\dagger a}$	**291.6**	**< 0.001**	**4**

Supplemental Figure 3. Summary of statistical analyses presented in Figure 4 (main text). Bold values: $p < 0.05$ and underlined values: $p < 0.1$. a = analysed using one-way ANOVA, b = analysed using a Kruskal-Wallis test, * = analysed on log-transformed data, † = analysed using white-adjusted ANOVAs, ‡ = analysed on square-root-transformed data.

Response	F/χ^2	*p-value*	*df*
Complex damage			
$Integral^{\dagger a}$	**42.39**	**< 0.001**	**2**
$t_{onset}{}^{a}$	0.99	0.396	2
$Duration^{a}$	1.58	0.239	2
$Shape^{a}$	2.58	0.109	2
Real herbivory			
$t_{onset}{}^{b}$	**18.07**	**0.001**	**4**
$Duration^{\dagger\ddagger a}$	**75.61**	**< 0.001**	**4**
$Shape^{a}$	**20.95**	**< 0.001**	**4**

Supplemental Table 4. Summary of statistical analyses presented in Supplemental figures 1 and 2. Bold values: $p < 0.05$ and underlined values: $p < 0.1$. a = analysed using one-way ANOVA, b = analysed using a Kruskal-Wallis test, * = analysed on log-transformed data, † = analysed using white-adjusted ANOVAs, ‡ = analysed on square-root-transformed data.

Response	F/χ^2	*p-value*	*df*
<u>*Green leaf volatiles*</u>			
t_{onset} ‡a	0.59	0.584	2
$Duration$ a	**34.02**	**< 0.001**	**2**
$Shape$ a	**6.78**	**0.029**	**2**
<u>*Gene expression*</u>			
t_{onset} ‡a	2.18	0.133	3
$Duration$ †a	**29.92**	**< 0.001**	**3**
$Shape$ a	<u>2.95</u>	<u>0.067</u>	<u>3</u>

Appendix 1.

Title: Quantitative modelling of biological response dynamics reveals novel patterns in plant volatile signalling

Authors: Jamie M. Waterman*†[1,2], Gareth J. Moore†[3], Loren K. Amdahl-Culleton[3], Sara Hoefer[2], Matthias Erb[2]

Affiliations: [1]Discipline of Botany, School of Natural Sciences, Trinity College Dublin, Dublin, Ireland [2]Institute of Plant Sciences, University of Bern, Bern, Switzerland

[3]Independent

*Corresponding author. Email: watermaj@tcd.ie

†Authors contributed equally to this work

Practical Guide to Fitting the Response Model in Python, R, and Excel

This provides a straightforward workflow to apply the response model to experimental time-series data. Each section (Python, R, Excel) can be read independently.

The goal is simple: given a time vector and a response vector, fit the model and extract the derived quantities (shape, duration, total integral).

To apply the model, you only need two data vectors: **time** and **response**. Provide rough starting values or bounds for the four parameters, then run the fitting procedure in your chosen environment (Python, R, or Excel). The steps are the same everywhere:

1. Load or enter your time and response data
2. Set initial parameter guesses or bounds
3. Run the optimiser (Python: DE→SLSQP; R: DEoptim→nloptr; Excel: Solver)
4. Check the fitted curve against your raw data
5. Use the fitted parameters to compute the derived quantities (shape, duration, and total integral)

Python

Define the Model and Fitting Function

This section defines the components needed to run the model:

1. The model, which evaluates the response for any set of parameters.
2. Helper functions that compute the derived quantities (shape, duration, total integral).
3. The fitting function, which estimates the four parameters from data.

The model is a direct implementation of the form described in the manuscript. A gamma-shaped rise and decay captures the response dynamics, while a logistic onset term smooths the beginning of the curve to improve numerical stability. The helper functions compute the analytical quantities defined in the paper.

The main fitting routine `fit_response_curve` takes three inputs: `time`, `response`, and a set of parameter bounds. These bounds can be estimated visually:

- `t_onset` : where the rise begins
- `t_peak` : where the maximum occurs
- `t_mean` : a point on the decay tail
- `R_peak` : approximate peak height

The fitting proceeds in two steps. A Differential Evolution search explores the full parameter space without relying on good initial guesses. A constrained SLSQP refinement then improves accuracy while ensuring valid parameter ordering (t_onset < t_peak < t_mean). The result is a dictionary containing the four optimised parameters.

```python
import numpy as np
from scipy.optimize import differential_evolution, minimize, Bounds
from scipy.special import gamma

# ----------------------------------------------------
# Model and helper functions
# ----------------------------------------------------

def model(t, R_peak, t_peak, t_onset, t_mean, epsilon=0.1):
    alpha = (t_mean - t_onset) / (t_mean - t_peak)
    beta = t_mean - t_peak
    t_adj = t - t_onset

    # np.clip prevents negative or zero values inside the power-law term.
    # Without this, early-time evaluations can cause (-ve)**fraction -> NaNs.
    core = ((np.clip(t_adj, 1e-10, None) / (t_peak - t_onset)) ** (alpha - 1)) * \
           np.exp(-(t_adj - (t_peak - t_onset)) / beta)

    # Logistic "ramp" smooths the onset (avoids a discontinuous corner at t_onset)
    # making the function differentiable for gradient-based optimizers.
    ramp = 1 / (1 + np.exp(-(t - t_onset) / epsilon))

    model_pred = R_peak * ramp * core

    # Replace NaN/inf values that appear with bad parameters.
    # Forces the model to stay finite, stabilizing optimization.
    model_pred = np.nan_to_num(model_pred, nan=0.0, posinf=0.0, neginf=0.0)

    return model_pred
```

```python
def shape(t_onset, t_peak, t_mean):
    denominator = t_mean - t_onset
    if denominator == 0:
        raise ValueError("t_mean and t_onset must not be equal to avoid division by zero.")
    return (t_mean - t_peak) / denominator


def duration(t_onset, t_peak, t_mean):
    return t_mean - t_onset


def total_integral_model(R_peak, t_peak, t_onset, t_mean):
    alpha = (t_mean - t_onset) / (t_mean - t_peak)
    beta = t_mean - t_peak
    t0 = t_peak - t_onset

    # gamma(alpha) is the Gamma function, generalizes factorial.
    A = R_peak * (t0 ** (1 - alpha)) * np.exp(t0 / beta)

    return A * (beta ** alpha) * gamma(alpha)


def fit_response_curve(time, response, param_config):
    param_names = ['R_peak', 't_peak', 't_onset', 't_mean']
    bounds_list = [(param_config[n]['min'], param_config[n]['max']) for n in param_names]

    def objective(x):
        params = dict(zip(param_names, x))
        return np.sum((model(time, **params) - response) ** 2)

    # Constraints enforce temporal ordering:
    # t_onset < t_peak < t_mean
    constraints = [
        lambda x: (x[3] - x[1]) - 0.1 * (x[3] - x[2]),  # mean - peak >= 10% of mean - onset
        lambda x: x[1] - x[2] - 0.1,                    # peak must follow onset
        lambda x: x[3] - x[1] - 0.1,                    # mean must follow peak
    ]

    constraints = [{'type': 'ineq', 'fun': c} for c in constraints]

    try:
        # Step 1: Differential Evolution (global)
        de_result = differential_evolution(
            objective,
            bounds=bounds_list,
            strategy='best1bin',
            maxiter=100,
            polish=False
        )

        # Step 2: SLSQP (local, constrained)
        local_result = minimize(
            objective,
            de_result.x,
            method='SLSQP',
            bounds=Bounds(*zip(*bounds_list)),
            constraints=constraints,
            options={'maxiter': 2000}
```

```
        )

        result_x = local_result.x if local_result.success else de_result.x

    except Exception as e:
        print(f"Optimization error: {e}")
        return None

    return dict(zip(param_names, result_x))
```

Fit the model

To run the workflow, provide arrays for time and response, set reasonable bounds, and call `fit_response_curve`. The fitted parameters can then be used to generate a model prediction and to compute shape, duration, and total integral.

A plot of raw versus fitted data helps assess quality. A good fit should capture the onset, peak position, and overall decay shape. Large systematic deviations usually indicate that bounds were too restrictive or the data deviate from model assumptions.

```
import numpy as np
import matplotlib.pyplot as plt

# ----------------------------------------------------
# Example data
# ----------------------------------------------------

time = np.array([
    -1.0, -0.5, 0.0, 0.5, 1.0, 1.5, 2.0, 2.5, 3.0, 3.5,
    4.0, 4.5, 5.0, 5.5, 6.0, 6.5, 7.0, 7.5, 8.0, 8.5,
    9.0, 9.5, 10.0, 10.5, 11.0, 11.5, 12.0, 12.5, 13.0, 13.5,
    14.0, 14.5, 15.0, 15.5, 16.0, 16.5, 17.0, 17.5, 18.0, 18.5,
    19.0, 19.5, 20.0, 20.5, 21.0, 21.5, 22.0
])

response = np.array([
    -0.54, 1.062, 0.205, 0.158, -0.82, 3.233, 15.25, 33.215, 47.672, 53.405,
    57.718, 55.81, 52.93, 53.346, 44.75, 42.752, 36.476, 36.371, 32.15, 29.553,
    27.149, 23.344, 18.599, 15.548, 14.316, 11.673, 9.89, 8.171, 8.574, 7.866,
    7.178, 5.328, 5.651, 4.508, 2.82, 2.063, 3.402, 2.15, -0.062, 0.83,
    0.435, 2.143, 0.198, 1.669, 0.046, -0.256, 0.709
])

# ----------------------------------------------------
# Parameter configuration
# ----------------------------------------------------

param_config = {
    'R_peak':   {'min': 40, 'max': 80},
    't_peak':   {'min': 2,  'max': 7},
    't_onset':  {'min': 0,  'max': 3},
    't_mean':   {'min': 5,  'max': 12},
}

# ----------------------------------------------------
# Fit the curve
```

```python
# ----------------------------------------------------

fit = fit_response_curve(time, response, param_config)
R_peak, t_peak, t_onset, t_mean = fit.values()

# Compute metrics
shape_val = shape(t_onset, t_peak, t_mean)
duration_val = duration(t_onset, t_peak, t_mean)
integral_val = total_integral_model(R_peak, t_peak, t_onset, t_mean)

# Create fitted curve
fitted = model(time, R_peak, t_peak, t_onset, t_mean)

# ----------------------------------------------------
# Print results
# ----------------------------------------------------

print("\n=== Fitted Parameters ===")
for k, v in fit.items():
    print(f"{k:8s}: {v:8.4f}")

print("\n=== Calculated Parameters ===")
print(f"Shape:     {shape_val:.4f}")
print(f"Duration:  {duration_val:.4f}")
print(f"Integral:  {integral_val:.4f}")

# ----------------------------------------------------
# Plot results
# ----------------------------------------------------

plt.figure(figsize=(10, 5))
plt.plot(time, response, 'o', label="Data", ms=5)
plt.plot(time, fitted, '-', label="Fitted Model", lw=2)
plt.xlabel("Time")
plt.ylabel("Response")
plt.legend()
plt.grid(alpha=0.3)
plt.title("Model Fit")
plt.show()
```

Output: Python

The printed results show the four fitted parameters and the derived quantities:

- `R_peak` : fitted peak height
- `t_onset` , `t_peak` , `t_mean` : timing of the main phases
- `Shape` , `Duration` , `Integral` : derived measures of the response

The accompanying plot confirms whether the fitted curve follows the raw data.

```
=== Fitted Parameters ===
R_peak  :  56.0646
t_peak  :   4.2280
t_onset :   1.7252
t_mean  :   6.8144
=== Calculated Parameters ===
Shape:     0.5082
Duration:  5.0892
Integral:  388.7458
```

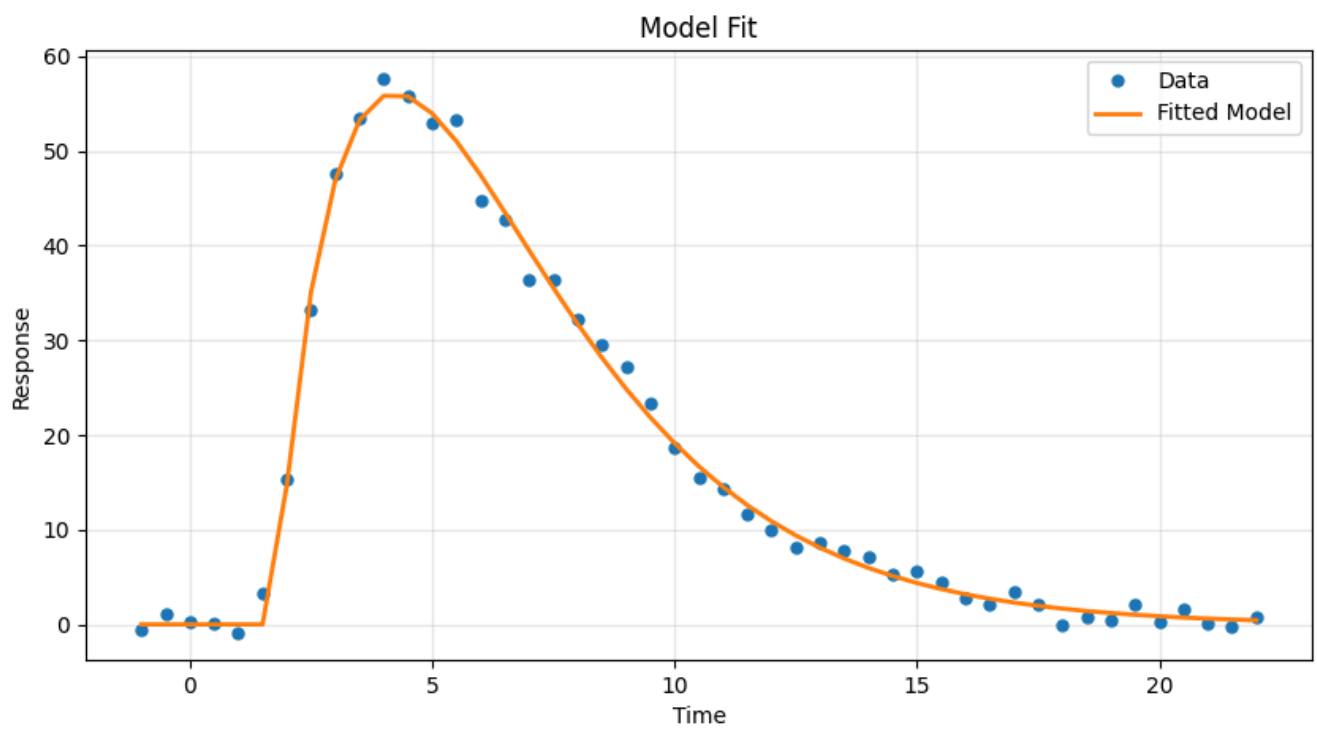

R: Model and Fitting Functions

This section provides a complete workflow for fitting the response model in R. It includes three components:

1. The model function, which computes the predicted response at each time point.
2. Helper functions that calculate the derived quantities (shape, duration, total integral).
3. A fitting function that estimates the four parameters from experimental data.

The model is a direct implementation of the analytical form described in the manuscript. It combines a gamma-shaped rise and decay with a logistic onset term, which smooths the beginning of the curve and stabilises numerical optimisation. The helper functions use the fitted parameters to compute the analytical descriptors of interest.

The fitting routine `fit_response_curve` takes three inputs:

- `time` : numeric vector of time values
- `response` : numeric vector of observed responses
- `param_config` : named list giving lower and upper bounds for each parameter

These bounds can be chosen by eye:

- `t_onset` : near the initial rise
- `t_peak` : near the maximum
- `t_mean` : in the decay region
- `R_peak` : near the observed peak height

The optimisation proceeds in two stages. A `DEoptim` global search explores the parameter space without relying on good initial guesses. A local refinement using `optim` (L-BFGS-B) then improves accuracy while keeping parameters within their bounds. Simple inequality checks enforce the required temporal order (`t_onset` < `t_peak` < `t_mean`). The function returns all four fitted parameters in a named list.

```
library(DEoptim)
library(stats)
library(pracma)
library(ggplot2)

# ====================================================
# Model and helper functions
# ====================================================

model <- function(t, R_peak, t_peak, t_onset, t_mean, epsilon = 0.1) {
    alpha <- (t_mean - t_onset) / (t_mean - t_peak)
    beta  <- t_mean - t_peak
    t_adj <- t - t_onset

    core <- ((pmax(t_adj, 1e-10) / (t_peak - t_onset))^(alpha - 1)) *
        exp(-(t_adj - (t_peak - t_onset)) / beta)

    ramp <- 1 / (1 + exp(-(t - t_onset) / epsilon))

    pred <- R_peak * ramp * core
    pred[!is.finite(pred)] <- 0

    return(pred)
}

shape_fun <- function(t_onset, t_peak, t_mean) {
```

```r
    denom <- t_mean - t_onset
    if (denom == 0) stop("t_mean == t_onset")
    return((t_mean - t_peak) / denom)
}

duration_fun <- function(t_onset, t_peak, t_mean) {
    return(t_mean - t_onset)
}

total_integral_model <- function(R_peak, t_peak, t_onset, t_mean) {
    alpha <- (t_mean - t_onset) / (t_mean - t_peak)
    beta  <- t_mean - t_peak
    t0    <- t_peak - t_onset
    A <- R_peak * (t0^(1 - alpha)) * exp(t0 / beta)
    return(A * (beta^alpha) * gamma(alpha))
}

# ====================================================
# Fitting function
# ====================================================

fit_response_curve <- function(time, response, param_config) {
    param_names <- c("R_peak", "t_peak", "t_onset", "t_mean")
    lower <- sapply(param_config, function(x) x$min)
    upper <- sapply(param_config, function(x) x$max)

    objective <- function(x) {
        names(x) <- param_names
        pred <- model(time,
                      x["R_peak"], x["t_peak"],
                      x["t_onset"], x["t_mean"])
        sum((pred - response)^2)
    }

    constraint_valid <- function(x) {
        t_onset <- x[3]
        t_peak  <- x[2]
        t_mean  <- x[4]
        c1 <- (t_mean - t_peak) - 0.1 * (t_mean - t_onset)
        c2 <- t_peak - t_onset - 0.1
        c3 <- t_mean - t_peak - 0.1
        return(all(c(c1, c2, c3) >= 0))
    }

    objective_constrained <- function(x) {
        if (!constraint_valid(x)) return(1e12)
        objective(x)
    }

    de_out <- DEoptim(
        fn = objective_constrained,
        lower = lower,
        upper = upper,
        DEoptim.control(
            itermax = 100,
            trace = FALSE
        )
    )
    x_de <- de_out$optim$bestmem
```

```r
    penalty_obj <- function(x) {
        penalty <- if (!constraint_valid(x)) 1e10 else 0
        objective(x) + penalty
    }

    local_out <- optim(
        par = x_de,
        fn = penalty_obj,
        method = "L-BFGS-B",
        lower = lower,
        upper = upper,
        control = list(maxit = 2000)
    )

    x_final <- local_out$par
    names(x_final) <- param_names
    return(as.list(x_final))
}
```

Usage Example: R

The following example shows the complete workflow: providing time and response vectors, defining parameter bounds, running the fitting routine, and computing the derived quantities. After fitting, the parameters are used both to generate the model prediction and to calculate shape, duration, and integral.

A plot comparing the raw data with the fitted curve provides an immediate check on fit quality. Good fits typically recover the onset, location of the peak, and overall decay structure, though small deviations in noisy regions are expected.

```r
# ====================================================
# Example data
# ====================================================

time <- c(
  -1.0, -0.5, 0.0, 0.5, 1.0, 1.5, 2.0, 2.5, 3.0, 3.5,
  4.0, 4.5, 5.0, 5.5, 6.0, 6.5, 7.0, 7.5, 8.0, 8.5,
  9.0, 9.5, 10.0, 10.5, 11.0, 11.5, 12.0, 12.5, 13.0, 13.5,
  14.0, 14.5, 15.0, 15.5, 16.0, 16.5, 17.0, 17.5, 18.0, 18.5,
  19.0, 19.5, 20.0, 20.5, 21.0, 21.5, 22.0
)

response <- c(
  -0.54, 1.062, 0.205, 0.158, -0.82, 3.233, 15.25, 33.215, 47.672, 53.405,
  57.718, 55.81, 52.93, 53.346, 44.75, 42.752, 36.476, 36.371, 32.15, 29.553,
  27.149, 23.344, 18.599, 15.548, 14.316, 11.673, 9.89, 8.171, 8.574, 7.866,
  7.178, 5.328, 5.651, 4.508, 2.82, 2.063, 3.402, 2.15, -0.062, 0.83,
  0.435, 2.143, 0.198, 1.669, 0.046, -0.256, 0.709
)

# ====================================================
# Parameter config
# ====================================================

param_config <- list(
  R_peak  = list(min = 40, max = 80),
```

```r
  t_peak  = list(min = 2,  max = 7),
  t_onset = list(min = 0,  max = 3),
  t_mean  = list(min = 5,  max = 12)
)

# ====================================================
# Fit curve
# ====================================================

fit <- fit_response_curve(time, response, param_config)

R_peak  <- fit$R_peak
t_peak  <- fit$t_peak
t_onset <- fit$t_onset
t_mean  <- fit$t_mean

shape_val    <- shape_fun(t_onset, t_peak, t_mean)
duration_val <- duration_fun(t_onset, t_peak, t_mean)
integral_val <- total_integral_model(R_peak, t_peak, t_onset, t_mean)

fitted <- model(time, R_peak, t_peak, t_onset, t_mean)

# ====================================================
# Print results
# ====================================================

cat("\n=== Fitted Parameters ===\n")
print(fit)

cat("\n=== Calculated Parameters ===\n")
cat("Shape:    ", shape_val, "\n")
cat("Duration: ", duration_val, "\n")
cat("Integral: ", integral_val, "\n")

# ====================================================
# Plot
# ====================================================

df <- data.frame(time = time, response = response, fitted = fitted)

ggplot(df, aes(time)) +
  geom_point(aes(y = response), color = "blue") +
  geom_line(aes(y = fitted), color = "red") +
  theme_minimal() +
  labs(
    title = "Model Fit",
    x = "Time",
    y = "Response"
  )
```

Output: R

The fitted parameters and derived quantities are printed in a straightforward format:

- `R_peak` : fitted maximum response
- `t_onset` , `t_peak` , `t_mean` : timing of the response phases
- `Shape` , `Duration` , `Integral` : analytical quantities derived from the fitted model

The plot confirms visually whether the fitted curve captures the key features of the observed data.

```
=== Fitted Parameters ===
$R_peak
[1] 56.06604
$t_peak
[1] 4.228
$t_onset
[1] 1.725197
$t_mean
[1] 6.814355

=== Calculated Parameters ===
Shape:     0.5082089
Duration:  5.089157
Integral:  388.7487
```

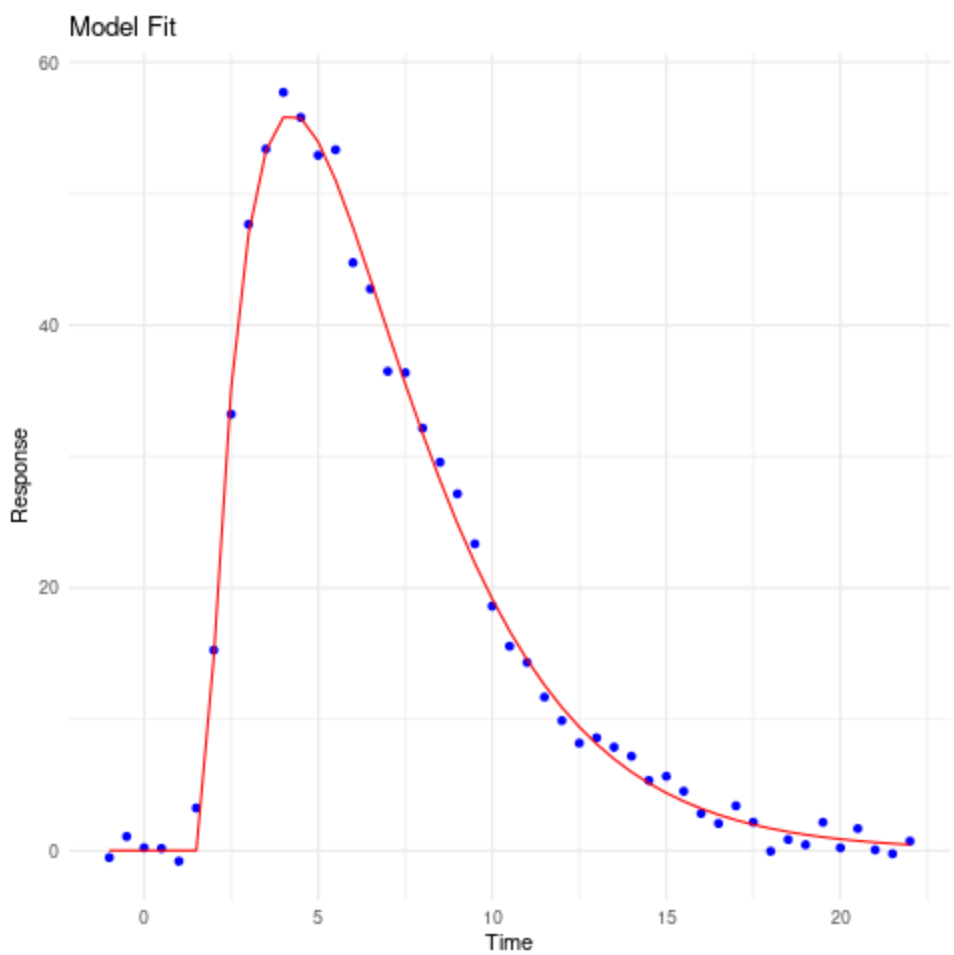

Excel: Model and Fitting Functions

Excel provides a simple, visual way to use the model. The full workflow is:

1. Enter your time and response data
2. Enter initial parameter guesses and provide min/max bounds for each parameter
3. Compute the model prediction
4. Compute squared errors and SSE
5. Use Solver to optimise the parameters
6. Compute the derived quantities (shape, duration, integral)

Step 1:

Place your measurements into two columns:

```
"Our raw data time and response values in the following columns."
time = A
response = B
```

Step 2:

Reserve cells for the four parameters and their bounds, entering rough starting velues:

```
"Our parameter values in the following cells."
R_peak   = G2, R_peak_min = H2,  R_peak_max = I2
t_peak   = G3, t_peak_min = H3,  t_peak_max = I3
t_onset  = G4, t_onset_min = H4, t_onset_max = I4
t_mean   = G5, t_mean_min = H5,  t_mean_max = I5
```

F	G	H	I
parameter	value	min	max
R_peak	50	40	80
t_peak	4	2	7
t_onset	1	0	3
t_mean	7	5	12
SSE	921.7242		

Step 3:

In **C2**, enter the model formula and drag down:

```
"Model prediction for each time value A2:A…."
model = $G$2 *
  ( MAX( A - $G$4 , 1E-10 ) / ($G$3 - $G$4) ) ^
    ( ( $G$5 - $G$4 ) / ( $G$5 - $G$3 ) - 1 ) *
  EXP( - ( (A2 - $G$4) - ($G$3 - $G$4) ) / ($G$5 - $G$3) )

"Model can be used to fill a column with predicted values."
model = C
```

Column **C** now contains the predicted values.

Step 4:

In order to fit the model, we first need a way to measure how far the current parameter guesses are from the actual data. We do this by calculating the **squared error** between the observed response and the model prediction at each time point.

```
"The square error is calculated from each raw and model response value"
sq_err = D = (B - C)^2
```

Drag this down to fill the column.

To combine all point-wise errors into a single value that Solver can minimise, compute the sum of squared errors (SSE) in G10:

```
"Sum the square errors."
SSE = $G$10 = SUM(D2:D...)
```

The SSE reflects how well the current parameters match the data: lower values indicate a better fit. Solver will adjust the parameters to minimise this value.

Step 5:

Open **Data** → **Solver** and configure the following:

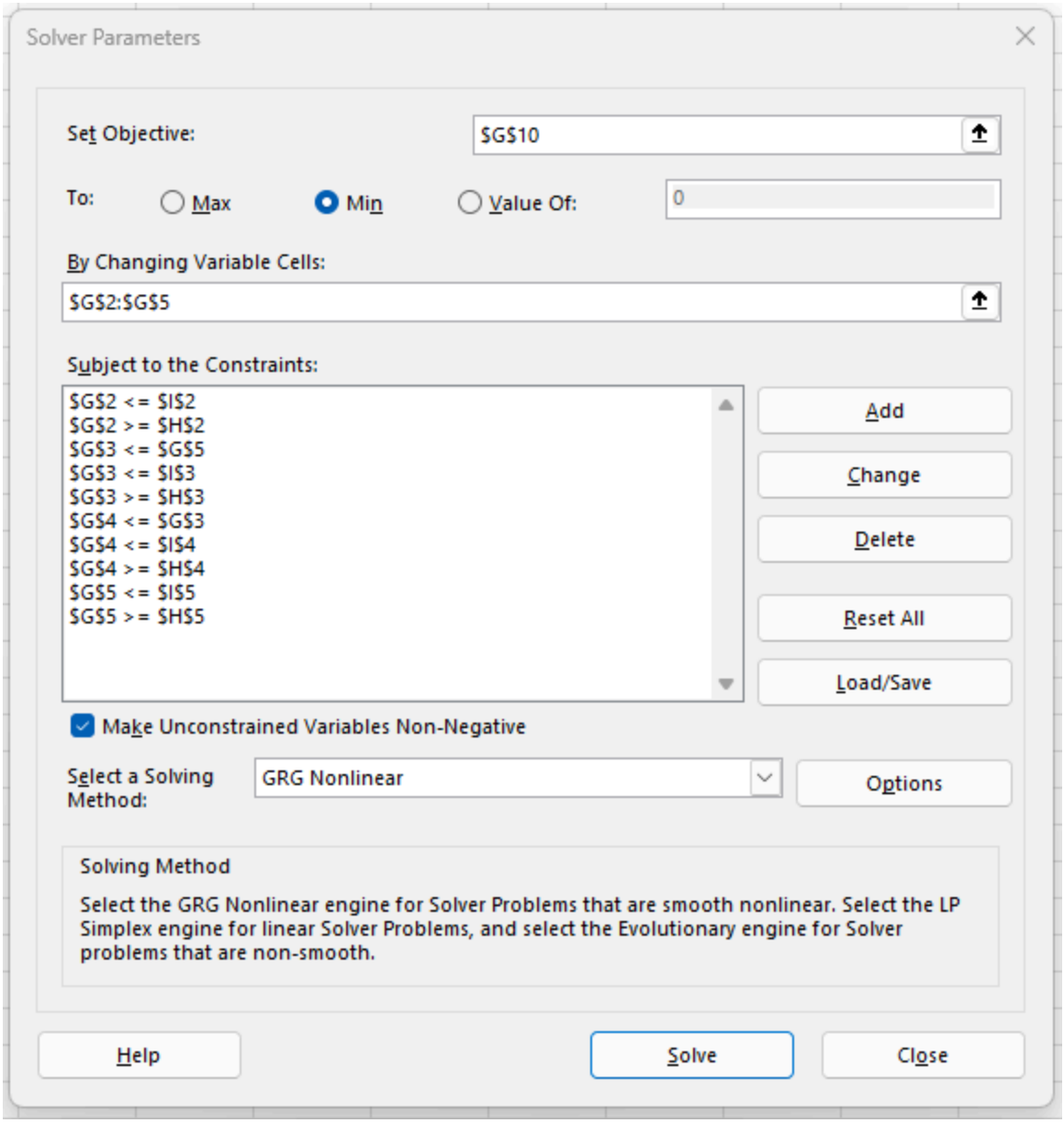

Objective

- `Set Objective` : `G10`
- `To` : Min
  Variable cells
- `By Changing Variable Cells` : `G2:G5`

Constraints
Add both parameter bounds and temporal ordering:
`Subject to the Constraints` :

- `G2 >= H2` and `G2 <= I2`
- `G3 >= H3` and `G3 <= I3`
- `G4 >= H4` and `G4 <= I4`
- `G5 >= H5` and `G5 <= I5`

Temporal ordering

- `G4 < G3` (onset before peak)
- `G3 < G5` (peak before mean)

Method

- `Select a Solving Method`: `GRG Nonlinear`

Click `Solve`.

If successful, Solver updates cells `G2–G5` with the best-fitting parameters.

F	G	H	I
parameter	value	min	max
R_peak	56.12524	40	80
t_peak	4.218756	2	7
t_onset	1.759892	0	3
t_mean	6.829637	5	12
SSE	72.25635		

Step 6:

Once Solver converges, compute the analytical quantities that characterise the fitted response.

In any convenient column or cells:

```
"Calculated parameter cells filled based on the parameter values."
shape = ($G$5 - $G$3) / ($G$5 - $G$4)
duration = $G$5 - $G$4
integral = $G$2 *
  ( ($G$3 - $G$4) ^ ( 1 - ( ($G$5 - $G$4) / ($G$5 - $G$3) ) ) ) *
  EXP( ( $G$3 - $G$4 ) / ( $G$5 - $G$3 ) ) *
  ( ($G$5 - $G$3) ^ ( ($G$5 - $G$4) / ($G$5 - $G$3) ) ) *
  GAMMA( ( $G$5 - $G$4 ) / ( $G$5 - $G$3 ) )
```

These update automatically if the parameter cells change.

Output: Excel

After running Solver, the fitted parameter values appear in the parameter cells, and the SSE decreases accordingly. The model prediction column updates automatically, as do the derived quantities (shape, duration, integral). These values provide a direct summary of the fitted response.

A plot comparing the observed data with the model prediction gives a visual check of fit quality. A successful fit will show the model curve following the rise, peak, and decay of the measured response, as illustrated in the example screenshot.
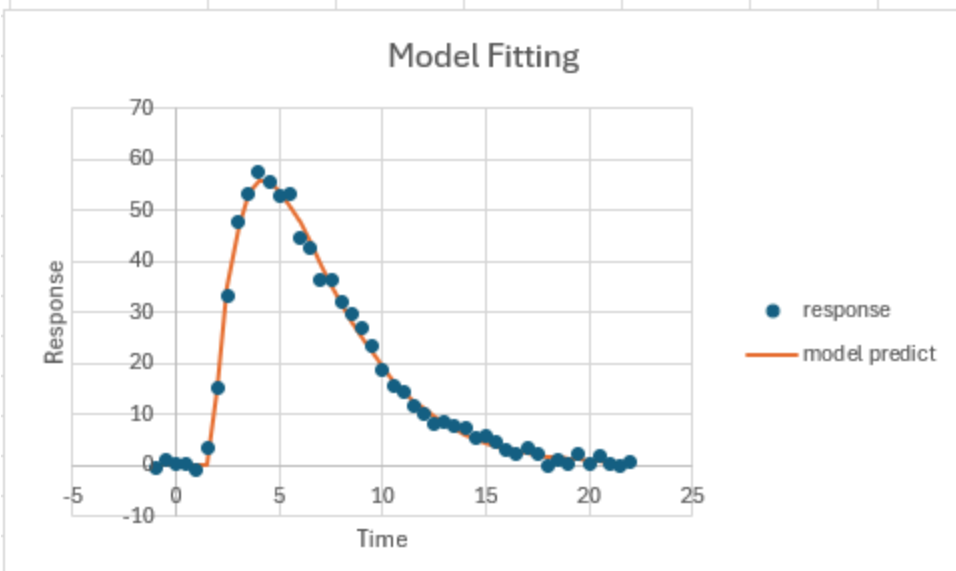
F	G	H	I	J	K	L
parameter	value	min	max			
R_peak	56.12524	40	80			
t_peak	4.218756	2	7			
t_onset	1.759892	0	3			
t_mean	6.829637	5	12			
SSE	72.25635					
shape	0.514993					
duration	5.069745					
integral	388.3996